

Geometry-Aware Scene Configurations for Novel View Synthesis

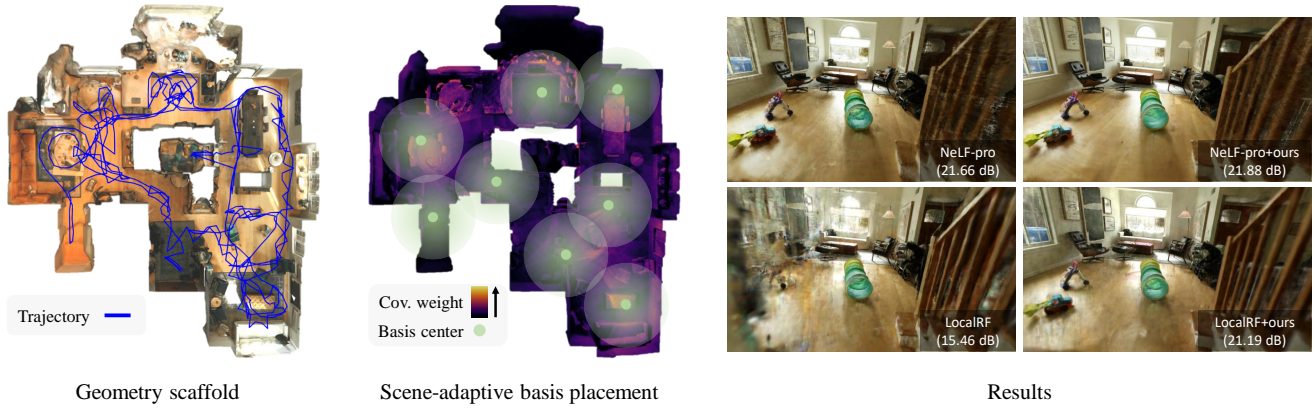
Minkwan Kim¹Changwoon Choi¹Young Min Kim^{1,2}¹ Dept. of Electrical and Computer Engineering, Seoul National University² Interdisciplinary Program in Artificial Intelligence and INMC, Seoul National University

Figure 1. **Geometry-aware basis configuration and novel view synthesis results.** After recording measurement statistics as coverage weights on geometry scaffold, we find optimal basis positions and training-view configurations in indoor environments.

Abstract

We propose scene-adaptive strategies to efficiently allocate representation capacity for generating immersive experiences of indoor environments from incomplete observations. Indoor scenes with multiple rooms often exhibit irregular layouts with varying complexity, containing clutter, occlusion, and flat walls. We maximize the utilization of limited resources with guidance from geometric priors, which are often readily available after pre-processing stages. We record observation statistics on the estimated geometric scaffold and guide the optimal placement of bases, which greatly improves upon the uniform basis arrangements adopted by previous scalable scene representations. We also suggest scene-adaptive virtual viewpoints to compensate for geometric deficiencies inherent in view configurations in the input trajectory and impose the necessary regularization. We present a comprehensive analysis and discussion regarding rendering quality and memory requirements in several large-scale indoor scenes, demonstrating significant enhancements compared to baselines that employ regular placements.

1. Introduction

Recent advances in Neural Radiance Fields (NeRF) [27] enable casual users to obtain an immersive experience observing 3D objects or scenes only from image observations. The geometric information is implicitly encoded through the spatial distribution of density and radiance in a highly efficient manner. However, NeRF representations, along with various data structures [12, 28, 34, 37, 50], have limited expressive power to encompass the infinite resolution of large-scale scenes. Simply expanding the spatial range to unbounded scenes [1, 7, 53] cannot efficiently account for the complex layouts. Furthermore, synthesized results from hand-held observations of everyday environments often degrade due to the lack of measurement rays, compared to typical benchmarks composed of forward-facing views or surrounding views of objects within a bounding box.

To effectively model large-scale indoor scenes from hand-held trajectories, a systematic approach that accounts for the interplay between the scene geometry and camera viewpoints is needed. In many real-world scenarios, geometric priors are readily available. Conventional frameworks for novel-view synthesis first acquire measurements and train the neural volume offline using camera locations extracted from a structure-from-motion (SfM) [35] pipeline.

We can then obtain geometric scaffolds from existing neural implicit surface reconstruction methods and develop scene-adaptive strategies to significantly enhance reconstruction quality under confined resources.

We use geometric scaffolds to actively analyze the correlations between the scene geometry and the input observations, creating scene-adaptive spatial arrangements. As illustrated in Fig. 2, several previous works demonstrated combining multiple bases to represent the whole scene, where individual bases represent distributed regions [20, 25, 38, 40, 49]. The bases refer to spatial entities, such as NeRF blocks or feature grids, which may suffer from limited expressiveness in isolation. They have been allocated 1) based on camera trajectory [25, 49] or 2) by dividing scenes evenly in space [20, 38, 40], which does not consider the non-uniform nature of indoor geometry nor the measurements. Instead, we optimize the distribution of bases for the coverage of the input trajectory directly on the estimated geometry scaffolds, as demonstrated in Fig. 1. The resulting spatial arrangements are adaptive to the scene geometry and the measurement statistics, leading to an efficient scene representation.

Given the geometric scaffold and camera measurements, we also introduce a scene-adaptive geometric regularization strategy to guide optimization for desired regions. Observations rarely cover the whole scene exhaustively, especially when navigating through complex layouts. We use the obtained geometric scaffold to assess the deficiency within the acquired representation and locate virtual views that efficiently eliminate the prominent artifacts, as suggested by next-best-view planning [18, 30, 44]. Then, we extract depths in the selected virtual views to provide plausible supervision in unobserved regions [9, 13, 29, 33, 36, 41].

Our scene-adaptive strategies are applicable to various representations for novel-view synthesis and greatly enhance the quality of results of the given measurement trajectory. Our key contributions are summarized as follows:

- We propose efficient scene adaptation and training techniques for novel-view synthesis from pre-defined camera trajectories in large-scale indoor environments.
- We successfully accumulate the statistics of input observations within energy functions defined on the geometric scaffold from which we can optimize the positions of a limited set of bases.
- We guide optimization for sparsely captured regions using scene-aware virtual viewpoints, seamlessly blending them into a coherent representation.

We evaluate our approaches using two representative basis sets [25, 49] on real-world indoor scenes from the ScanNet++ [48] and Zip-NeRF [2] datasets and demonstrate effective performance enhancements in practical setups.

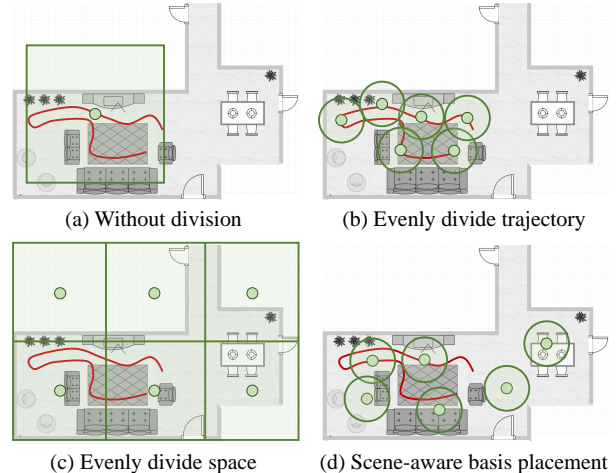


Figure 2. **Scene-splitting strategies.** (a) The original NeRF represents the entire scene with a single block. Scalable scene representations set multiple bases (b) evenly along the camera trajectory or (c) uniformly dividing the scene’s spatial extent. (d) We propose an adaptive approach based on scene configurations. Red curves denote camera trajectories and green dots mark the bases’ centers.

2. Related Work

Scene-adaptive capture and reconstruction The reconstruction quality of 3D representation depends heavily on the viewpoints from which the measurements are collected. Motivated by 3D scanning applications, next-best-view planning designs the best viewpoints to scan a 3D scene [44]. While pursuing uniform coverage can be a general approach [18], more advanced methods achieve high-quality reconstruction by minimizing the uncertainty based on the estimated underlying scene geometry [30, 45]. Several works also demonstrate performance enhancement in neural 3D scene representation by allocating more resources to regions with finer details [12, 22, 24, 50]. In this work, we suggest a scene-adaptive strategy for free-camera trajectory input, where we optimize the spatial arrangements for both scene representation and training views.

Scalable scene representation While NeRF excels at representing 3D scenes, it often struggles to accurately express large-scale environments. To model large-scale, unbounded scenes, recent approaches constitute the scene with several units of spatial structure, where each unit is modeled by a separate neural network [8, 20, 25, 38, 40]. However, relatively little work explores how to locate subsets of radiance fields, which we refer to as bases. Common approaches either regularly place bases along the camera trajectories [25, 49] or uniformly divide the scene region [20, 38, 40]. Instead, we adaptively consider the correlation between the scene geometry and camera observation to enhance the performance given limited resources.

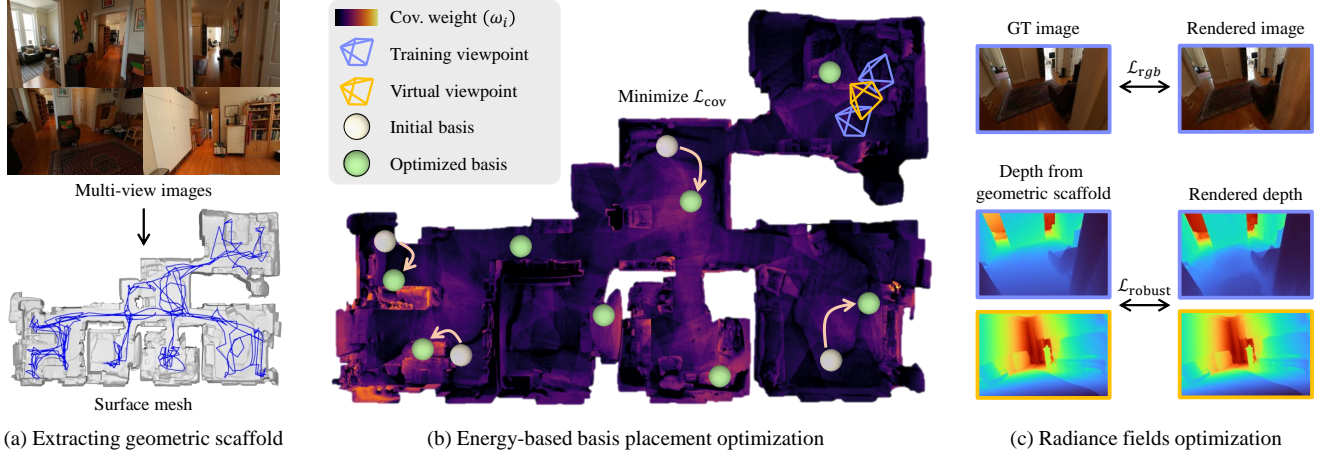


Figure 3. **Method overview.** (a) We first extract the geometric scaffold from multi-view image observation. (b) Then we define coverage weights w_i for surface points \mathbf{x}_i on the obtained mesh surface which consider both scene geometry and observation statistics. Starting from bases sampled along the camera trajectory using the FPS algorithm, we optimize their positions by minimizing energy function \mathcal{L}_{cov} . (c) Finally, we optimize radiance fields with RGB supervision, guided by geometric regularization on training and virtual viewpoints.

Geometric regularization for novel-view synthesis Fitting 3D scene structure is prone to overfitting and under-constrained conditions, leading to significantly degraded rendering quality for viewpoints far from input observations. Recent approaches notably reduce floating artifacts with monocular depth estimation [3, 31, 32], which may not be multi-view consistent. Possible misalignments can be adjusted by modeling scale ambiguities [4, 52] or multimodality of estimations [41]. On the other hand, coarse depths obtained from SfM [35] or depth sensors are noisy but can guide building the coherent scene representation. Groups of works [9, 33] model uncertainty for these settings, while SparseNeRF [13] enables regularization by only comparing the relative depth. NeRFVS [46] introduces the robust depth loss term for noisy and dense depth supervision. In contrast, we propose a geometric regularization method that leverages a 3D scaffold and adaptive virtual viewpoints, enabling robust training under limited views.

3. Method

Given free-trajectory images capturing a large indoor scene, our approach first extracts geometric scaffolds (Sec. 3.1). We use geometric scaffolds to optimize basis placements (Sec. 3.2), where each basis comprise local scene representation as described in Sec. 2. Then, based on geometry and observation statistics, we sample virtual views to be regularized and train radiance fields with depth supervision on both input and virtual views (Sec. 3.3).

3.1. Geometric Scaffolds

Given posed images, we obtain the surface mesh as we train for the radiance fields [14, 42, 47, 52]. NeRFs train a neu-

ral network that estimates a mapping function from 3D location $\mathbf{x} \in \mathbb{R}^3$ and viewing direction $\mathbf{d} \in \mathbb{R}^2$ to volume density $\sigma \in \mathbb{R}^+$ and color $\mathbf{c} \in \mathbb{R}^3$. Given N discrete points sampled along the ray \mathbf{r} , the color is rendered by the volume rendering equation given as follows:

$$\hat{C}(\mathbf{r}) = \sum_{i=0}^{N-1} T_i (1 - \exp(-\sigma_i \delta_i)) \mathbf{c}_i, \quad (1)$$

where $T_i = \exp(-\sum_{j=0}^{i-1} \sigma_j \delta_j)$ and δ_i denotes the distance between ray samples. The training loss for the network is the color difference between the rendered color \hat{C} and the pixel value of the training image C as follows:

$$\mathcal{L}_{rgb} = \|C(\mathbf{r}) - \hat{C}(\mathbf{r})\|_2^2. \quad (2)$$

We modify the original NeRF formulation and employ a recent implicit surface reconstruction model [52] to obtain geometric scaffolds. The network outputs signed distance fields (SDF) in addition to colors, which are converted to volume density. Then, we revise the volume rendering equation in Eq. (1) to estimate the depth of the neural implicit surface for each pixel:

$$\hat{D}(\mathbf{r}) = \sum_{i=0}^{N-1} T_i (1 - \exp(-\sigma_i \delta_i)) t_i, \quad (3)$$

where t_i is the distance from the sample to the origin. With input depths, we can apply additional depth loss as

$$\mathcal{L}_{depth} = \|D^*(\mathbf{r}) - \hat{D}(\mathbf{r})\|_2^2. \quad (4)$$

$D^* = \alpha D + \beta$ denotes undistorted depth, where α and β are scale and shift factors defined per frame.

After training, we obtain geometric scaffolds with the Marching Cubes algorithm [23] as visualized in Fig. 3 (a), and leverage the geometric prior in subsequent stages.

3.2. Basis Placement Optimization

This section introduces adaptively optimizing the basis distribution based on the scene geometry and camera trajectories, where the basis contributes to modeling local radiance fields. We define the coverage weights w_i that summarize the observation statistics on the geometric scaffold obtained from Sec. 3.1. At a point $\mathbf{x}_i \in \mathbb{R}^3$ sampled from the scaffold, the corresponding coverage weight w_i is calculated as

$$w_i = \sum_k \left(\frac{\hat{\mathbf{n}}_i \cdot (\mathbf{c}_k - \mathbf{x}_i)}{\|\mathbf{c}_k - \mathbf{x}_i\|^3} \right) \text{Vis}(\mathbf{c}_k \rightarrow \mathbf{x}_i). \quad (5)$$

$\text{Vis}(\mathbf{c}_k \rightarrow \mathbf{x}_i) \in \{0, 1\}$ denotes the point \mathbf{x}_i 's visibility from the camera \mathbf{c}_k . The weight term accumulates observations of the surface points from cameras, whose weights are inversely proportional to the squared distance to cameras and proportional to the inner product between the viewing vector and the surface normal $\hat{\mathbf{n}}_i$. Fig. 4 (a) illustrates the process of obtaining the coverage weight.

Then, we optimize bases positions $\mathbf{p}_j \in \mathbb{R}^3$ to best describe the accumulated coverage. We define the coverage-based loss term as follows:

$$\mathcal{L}_{\text{cov}} = \sum_i w_i \left(\frac{\|\mathbf{p}_{\mathcal{C}(i)} - \mathbf{x}_i\|^3}{\hat{\mathbf{n}}_i \cdot (\mathbf{p}_{\mathcal{C}(i)} - \mathbf{x}_i) + \epsilon} \right), \quad (6)$$

where $\epsilon \approx 0$ was added to the denominator for stable optimization. The loss term penalizes distances between the basis and the mesh points, weighted by the observation frequency using Eq. (5). We only consider the nearest basis position \mathbf{p}_j from the surface point \mathbf{x}_i , where the $\hat{\mathbf{n}}_i \cdot (\mathbf{p}_j - \mathbf{x}_i) > 0$, indicated as $j = \mathcal{C}(i)$. See the supplementary material for detailed information on Eq. (6). During the optimization process illustrated in Fig. 4 (b), each basis element shifts toward the frequently observed regions such that the fixed capacity of bases is distributed to balance covering densely populated ray samples. Therefore, our basis optimization strategy has advantages in covering measurements of indoor environments with limited resources.

The optimized basis positions \mathbf{p}_j serve as the position of spatial elements that constitute global radiance fields in parts. We demonstrate results with two representative basis configurations by mapping \mathbf{p}_j as the centroid of each NeRF block [8, 20, 25, 38, 40] or neural light field probe position of the NeLF-pro [49] representation. In both cases, a set of bases is assigned to regional partitions of the scene extent, and we can benefit from adaptive placement that achieves collaborative coverage. See Fig. 3 (b) for initial and optimized basis positions, and the supplementary material contains additional details and illustrations.

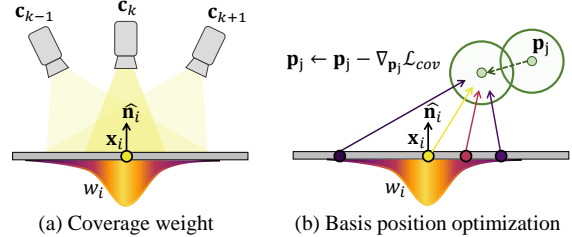


Figure 4. **Basis placement pipeline.** (a) After accumulating coverage weights w_i along surface points \mathbf{x}_i , (b) bases positions are updated using these weights and their distance from the surface.

NeRF blocks We modify the block locations to evaluate our placement strategy for multiple NeRF blocks. We set centroids of NeRF blocks at scene-adaptive basis positions while LocalRF [25] sequentially assigns NeRF blocks along the camera trajectory as shown in Fig. 2 (b). Other works suggest uniformly partitioning the spaces to distribute the blocks [20, 38, 40], which are demonstrated in Fig. 2 (c). The blocks are trained independently from rays emanating from the original input camera poses. We do not incorporate joint pose optimization to focus on the effect of block placements that respect ray distributions. As discussed in the result section, our proposed basis configuration can better describe necessary scene details contained within the input measurements.

While the detailed implementation for individual blocks may vary [8, 20, 25, 38, 40], we follow the original implementation in LocalRF [25] and represent the radiance as the sum of factorized tensor products of TensorRF [6] with the scene contraction of Mip-NeRF 360 [1]. Radiances in the overlapping area are blended from multiple blocks whose blending weights are inversely proportional to the distance between the camera position and centroid, following the Block-NeRF [38] implementation. We blend radiance values from, at most, two nearest NeRF blocks.

Neural lightfield probes NeLF-pro [49] is another approach that leverages local radiance fields to describe large-scale scenes. They decompose the scene representation into vector-matrix-matrix (VMM) factorization, also motivated by TensorRF [6]. Specifically, core factors (i.e., VM) encode the global features and are combined with basis factors (i.e., M) that encode local features. These factors are assigned as probes distributed in 3D space, whose locations are uniformly selected from input camera poses. The core factors are located at clustered positions resulting from K-means clustering among input poses, whereas the basis factors are positioned by the farthest point sampling (FPS). We propose the basis probe factors to be located at the optimized basis positions \mathbf{p}_j , which jointly considers the scene layout and the measurement statistics. We allocate core factors to be at

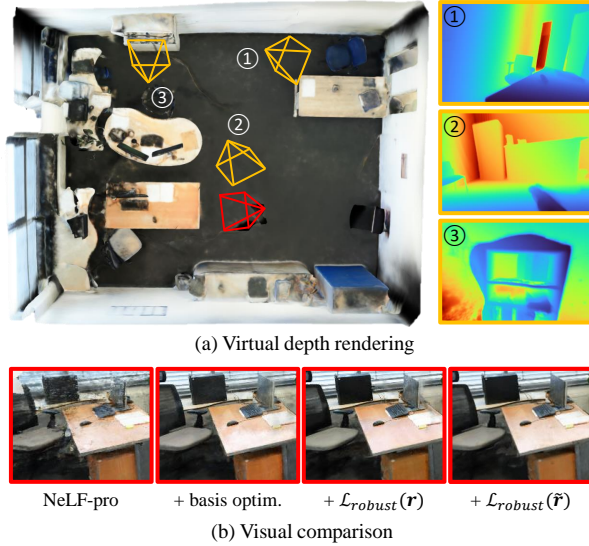


Figure 5. **Novel view geometric regularization.** (a) The illustration of selected virtual views (yellow) with rendered depth images on the right. (b) Test viewpoint images (red) show the effect of each component, added sequentially from left to right.

the cluster centers after applying K-means clustering on the basis probe locations.

When rendering, NeLF-pro aggregates features from a set of probes near the rendering view, which are decoded to volume densities and colors by a shallow MLP. In our setting, we find the closest set of probes for every sample on the ray, which may change within the same ray. We exploit the local radiance distribution specialized to the probes with sorting operations along the ray samples, which is detailed in the supplementary material.

3.3. Scene-Adaptive Geometric Regularization

We additionally incorporate geometric regularization to reduce floating artifacts, which are prominent in extreme viewpoint changes. While noisy, the estimated geometric scaffold from Sec. 3.1 can impose depth regularization to improve reconstruction quality. We use robust depth loss in Yang et al. [46] instead of the L2 loss introduced in Eq. (4):

$$\mathcal{L}_{\text{robust}} = \begin{cases} 0.5 \Delta D(\mathbf{r})^2, & \text{if } \Delta D(\mathbf{r}) < \gamma \\ \gamma^2 \left(0.5 + \log\left(\frac{\Delta D(\mathbf{r})}{\gamma}\right) \right), & \text{otherwise} \end{cases} \quad (7)$$

where $\Delta D(\mathbf{r}) = |D^*(\mathbf{r}) - \hat{D}(\mathbf{r})|$.

For each scene, we need additional regularization to estimate regions rarely covered by the input camera trajectories. We include supervision from novel views to cover the underlying scene efficiently. Starting from the original training cameras, we add viewpoints to build the set of training views S . The new views are progressively added to S from random samples $V \in \{v_1, v_2, \dots, v_n\}$ extracted from

empty space in the indoor region. Motivated by Xiao et al. [44], we define the selection criteria as follows:

$$v^* = \arg \max_{v \in V \setminus S} \left[\min_{s \in S} d(v, s) \right], \quad (8)$$

where $d(v, s)$ is the view distance defined as

$$d(v, s) = \|\mathbf{c}_v - \mathbf{c}_s\|^2 + \kappa \left(1 - \frac{\mathcal{A}_{vs}}{\max(\mathcal{A}_{vs})} \right). \quad (9)$$

The first term in Eq. (9) considers the distance between the next view candidate \mathbf{c}_v and the existing camera location \mathbf{c}_s , considering the spatial expansion. The second term employs similarity matrix \mathcal{A}_{vs} to account for scene diversity. The similarity matrix \mathcal{A}_{vs} contains the number of commonly observed feature points between view candidates $v \in V$ and sampled camera sets $s \in S$ such that the distance in Eq. (9) increases between dissimilar viewpoints. The features from the unseen views are estimated as projections of triangulated feature points from initial training sets, which are visible after considering the occlusion and camera frustums. The resulting depths from virtual viewpoints are demonstrated in Fig. 5 (a).

We use the combined set of viewpoints in S to provide additional supervision with the robust depth loss defined in Eq. (7). The total loss function to train each basis representation is given as follows:

$$\mathcal{L}_{\text{total}}(\tilde{\mathbf{r}}) = \mathcal{L}_{\text{rgb}}(\mathbf{r}) + \lambda_{\text{robust}} \mathcal{L}_{\text{robust}}(\tilde{\mathbf{r}}) + \lambda_{\text{reg}} \mathcal{L}_{\text{reg}}(\tilde{\mathbf{r}}), \quad (10)$$

where \mathbf{r} are the rays in the training views and $\tilde{\mathbf{r}}$ includes the sampled virtual views. \mathcal{L}_{reg} denotes other regularization terms, e.g., interlevel loss or distortion loss [1, 49]. Figure 3 (c) illustrates our geometric regularization, whose effects are compared in Fig. 5 (b) and the supplementary material.

4. Experiments

4.1. Experimental Setting

Dataset We evaluate our framework using two recent indoor scene datasets. (1) ScanNet++ [48] includes high-quality training and test image datasets with camera poses. (2) The Zip-NeRF dataset [2] comprises large-scale indoor and outdoor scenes with camera poses sampled from trajectories. See the supplementary material for dataset details.

Baselines We first include baselines that model 3D scenes and achieve novel view synthesis. (1) MonoSDF [51, 52] is a neural implicit surface reconstruction model trained using RGB, depth, and normal. (2) NeRFacto [39] combines hash encoding from Instant-NGP [28] and proposal sampling introduced in MipNeRF-360 [1]. For Zip-NeRF dataset, NeRFacto-big and NeRFacto-huge models were also tested with larger model capacity and training steps.

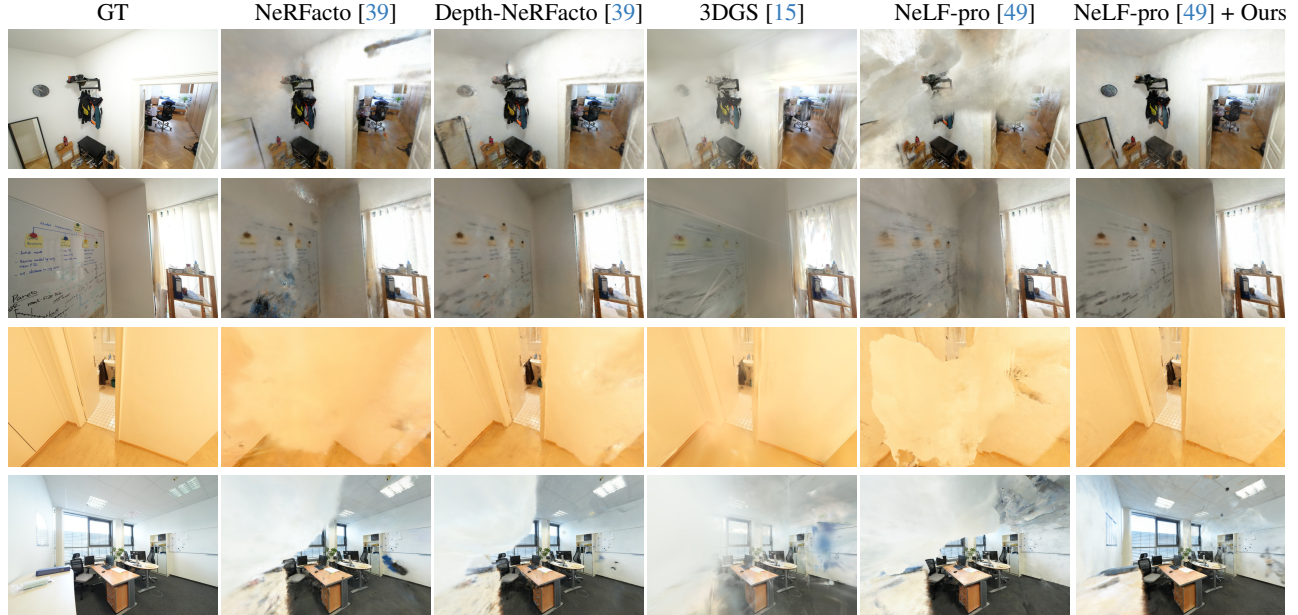


Figure 6. Qualitative results of novel view synthesis on ScanNet++ [48] dataset. Best viewed on screen.

(3) Depth-NeRFacto extends NeRFacto with depth supervision. We present results using SparseNeRF [13] depth supervision which showed the best performance among the available options. (4) 3DGS [15] is a state-of-the-art explicit scene representation method. Gaussians are initialized from the same feature points that were used in Sec. 3.3. (5) FSGS [55] is a recent version of 3DGS that includes depth regularization for sparse view inputs.

We also compare our approach to several scalable scene representations designed for modeling large-scale scenes. (6) Original NeLF-Pro [49] can be applied for both ScanNet++ and Zip-NeRF datasets, where the number of probe numbers and positions are tuned. (7) LocalRF [25] uses multiple NeRF blocks for scene representation. Since LocalRF requires a sequential input sequence, it can be evaluated only on Zip-NeRF datasets. (8) Mega-NeRF [40] uses a regular grid of multiple NeRF blocks. We only model Zip-NeRF scenes using 4×2 blocks, as the room-scale scenes of ScanNet++ do not benefit significantly. (9) Hierarchical-3DGS [16] is an extension of 3DGS to large-scale scenes. Depth regularization was used, and we conducted tests on both datasets. See the supplementary material for detailed configurations of our framework and baselines.

4.2. Results

In this section, we report the qualitative and quantitative results of our framework with comparative studies. For quantitative studies, we evaluated reconstructed image qualities using the peak-signal-to-noise ratio (PSNR), structure-similarity index measure (SSIM), and learned perceptual

Method	PSNR \uparrow	SSIM \uparrow	LPIPS \downarrow	Memory	Time
MonoSDF [52]	20.41	0.800	0.351	61 MB	6 h
NeRFacto [39]	20.52	0.793	0.352	65 MB	14 min
Depth-NeRFacto [39]	21.75	<u>0.808</u>	0.333	65 MB	17 min
ZipNeRF [2]	21.72	0.804	0.332	1.2 GB	42 min
3DGS [15]	21.26	0.797	0.305	164 MB	12 min
FSGS [55]	20.69	0.803	0.352	124 MB	27 min
DNGaussian [19]	19.26	0.780	0.483	156 MB	15 min
Hierarchical-3DGS [16]	20.57	0.771	0.335	793 MB	41 min
NeLF-pro [49]	<u>21.88</u>	0.795	0.367	89 MB	21 min
NeLF-pro [49] + Ours	22.52	0.814	<u>0.329</u>	89 MB	41 min

Table 1. Performance comparison on ScanNet++ [48] dataset. Our framework is tested using multiple neural feature grids. The upper table includes single-basis architectures while methods in the bottom leverage multiple basis. The first and second best results are highlighted in **bold** and underlined, respectively.

image patch similarity (LPIPS).

We first evaluate the performance of the novel view synthesis of our framework on the ScanNet++ dataset. In the results with the ScanNet++ dataset in Tab. 1, our work significantly outperforms other baselines in PSNR and SSIM without increasing memory usage. While our method uses the same number of parameters as NeLF-pro, it shows better reconstruction results with basis placement and geometry guidance accounting for scene configurations. Since 3DGS and its variants optimize scenes using primitives with extensive parameters, they are overfitted to training images and demonstrate good performance on densely observed regions. The common evaluation follows a practice in neural rendering evaluation protocol [1, 26, 27], and is conducted in an interpolation setting, where test views are frames uni-

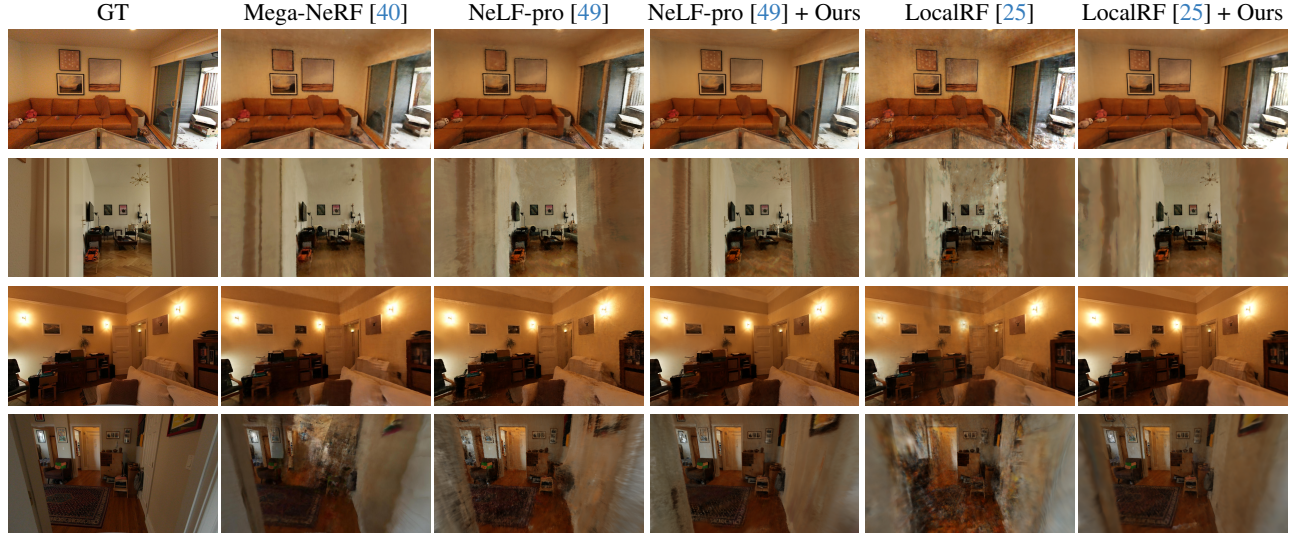


Figure 7. Qualitative results of novel view synthesis on Zip-NeRF [2] dataset. Best viewed on screen.

Method	PSNR \uparrow	SSIM \uparrow	LPIPS \downarrow	Memory	Time
MonoSDF [52]	20.61	0.733	0.459	61 MB	6 h
NeRFacto [39]	19.78	0.692	0.491	65 MB	14 min
NeRFacto [39]-Big	17.31	0.626	0.556	197 MB	1 h
NeRFacto [39]-Huge	17.41	0.627	0.514	211 MB	1.5 h
Depth-NeRFacto [39]	20.64	0.710	0.486	65 MB	17 min
ZipNeRF [2]	23.53	0.758	0.415	1.2 GB	42 min
3DGS [15]	<u>23.70</u>	0.807	0.347	225 MB	15 min
FSGS [55]	22.55	0.751	0.451	134 MB	30 min
DNGaussian [19]	19.38	0.694	0.679	170 MB	18 min
Mega-NeRF [40]	22.65	0.743	0.496	80 MB	48 h
Hierarchical-3DGS [16]	22.30	0.757	0.419	1.5 GB	56 min
NeLF-pro [49]	23.42	0.750	0.421	160 MB	24 min
NeLF-pro [49] + Ours	23.89	<u>0.762</u>	<u>0.400</u>	160 MB	46 min
LocalRF [25]	21.39	0.730	0.484	1.9 GB	6 h
LocalRF [25] + Ours	23.02	0.761	0.471	1.9 GB	6.5 h

Table 2. Performance comparison of methods on Zip-NeRF [2] dataset. Our framework is both tested on neural lightfield probes and NeRF blocks. The first and second best results are highlighted in **bold** and underlined, respectively.

formly sampled from training trajectories. However, the ScanNet++ dataset contains challenging test views that require view extrapolation, for which many conventional approaches, including 3DGS, have limited capability. Results in Fig. 6 include challenging view extrapolation scenarios where our framework outperforms other baselines.

To validate our framework using more challenging multi-room indoor scenarios, we demonstrate results with the Zip-NeRF dataset. Here, we validate our scheme using both NeLF-pro and LocalRF. As demonstrated in Tab. 2, our method greatly enhances both frameworks using multiple NeRF blocks and neural lightfield probes. Notably, combining LocalRF with our strategy achieves better reconstruction results than Mega-NeRF as shown in Fig. 7. While

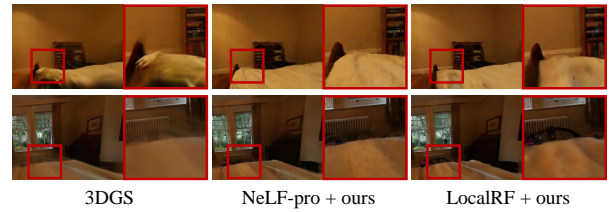


Figure 8. View extrapolation on Zip-NeRF [2] datasets.

LocalRF variants require more memory due to the TensorRF framework, Mega-NeRF uses less memory with the original NeRF implementation, taking over 2 days to train for up to 200k iterations. Meanwhile, Hierarchical-3DGS enables very fast rendering using 3D Gaussians within multiple chunks, leading to excessive memory consumption as the scene gets larger. To test for extrapolation tasks in Zip-NeRF datasets, which only include interpolation test settings, we rendered novel views from manually defined free camera trajectories. In this scenario, 3DGS suffers from degradation with sharp artifacts as demonstrated in Fig. 8. The additional results in the supplementary material demonstrate that our framework produces cleaner reconstructions in under-constrained regions, where even the SOTA 3DGS methods still exhibit artifacts.

In experiments with both datasets, our scene-adaptive strategy enables improved novel view synthesis in both interpolation and extrapolation scenarios with optimal basis placement and geometric regularization. As our method is built upon the original NeLF-pro and LocalRF framework, the memory usage is identical to that of the original implementation, given the same number of bases. See supplementary material for additional results.

Method	①	②	③	④	⑤	PSNR \uparrow	SSIM \uparrow	LPIPS \downarrow
NeLF-pro [49]	\times	\times	\times	\times	\times	21.88	0.795	0.367
	\times	\checkmark	\times	\times	\times	22.23	0.799	0.352
	\times	\checkmark	\checkmark	\times	\times	22.26	0.800	0.353
	\checkmark	\times	\times	\times	\times	22.22	0.807	0.349
	\checkmark	\checkmark	\times	\times	\times	22.42	0.810	0.342
\checkmark	\checkmark	\checkmark	\checkmark	\times	22.25	0.806	0.345	
+ Ours (full)	\checkmark	\checkmark	\checkmark	\times	\times	22.52	0.814	0.339
LocalRF [25]	\times	\times	\times	\times	\checkmark	21.39	0.725	0.484
	\times	\checkmark	\times	\times	\times	21.95	0.740	0.482
	\times	\checkmark	\checkmark	\times	\times	22.74	0.752	0.477
	\checkmark	\times	\times	\times	\checkmark	22.81	0.756	0.478
	\checkmark	\checkmark	\times	\times	\times	22.90	0.759	0.472
	\checkmark	\checkmark	\checkmark	\checkmark	\times	22.98	0.760	0.471
+ Ours (full)	\checkmark	\checkmark	\checkmark	\times	\times	23.02	0.761	0.471

Table 3. **Ablation studies on ScanNet++ [48] and Zip-NeRF [2] dataset.** We used multiple neural lightfield probes and nerf blocks for each case. Components marked by circled number denote the following: ①: basis optimization, ②: robust depth loss for training views, ③: novel view depth regularization, ④: random unobserved view depth regularization and ⑤: L2 depth loss for monocular depth estimation model.

Ablation study In Tab. 3, we compare image metrics for different cases to analyze the effect of our basis placement and geometric regularization strategy. For NeLF-pro and LocalRF variants, we test on ScanNet++ and Zip-NeRF dataset each. To check the effect of our main components, we conduct experiments for basis optimization, robust depth loss in Eq. (7) on training viewpoint, and robust depth loss for novel views. We observe that each component of our strategy contributes to the increase in reconstruction quality as shown in Tab. 3. To further verify the effect of our novel view depth regularization strategy, we compare our method to the depth regularization using the randomly sampled viewpoint as done in [29, 43]. Furthermore, with LocalRF variants, we compare the effect of depth supervision using a monocular depth [31] with the supervision using depth from a geometric scaffold. For monocular depth supervision, we add the regularization term defined in Eq. (4). Interestingly, our depth supervision strategy that uses geometric scaffold outperforms the original depth supervision using DPT [31], in the original LocalRF implementation. See supplementary materials for qualitative comparisons.

To further evaluate the robustness of our method across diverse scenarios, we analyze its performance under inaccurate geometry conditions and its applicability to certain outdoor scenes. As shown in the supplementary materials, our method effectively leverages geometric scaffolds, even when the provided geometry is imprecise.

Number of basis We analyze the performance of our framework with varying numbers of allocated bases. For both NeLF-pro and LocalRF variants, we tested on Zip-NeRF’s NYC dataset. NeLF-pro was tested with varying basis configurations: (4,2), (8,4), (16,4), (32,8), (64,16),

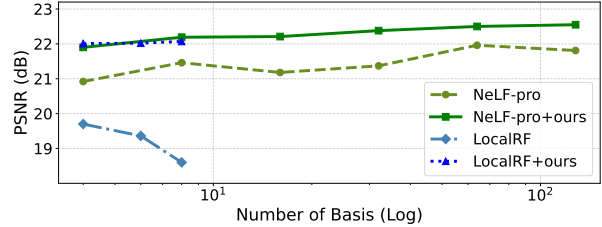


Figure 9. **PSNR comparison on a different number of bases.**

and (128,16), where the first value indicates the total number of bases and the second denotes the number of nearby bases. The number of core probes is fixed at 3. To adjust the number of NeRF blocks in the original LocalRF, we set different values for the maximum allowable drift before adding a new block. We examined PSNRs of the test views with the changing number of allocated bases in Fig. 9. Our framework robustly outperforms the baselines in every basis number. In LocalRF, NeRF blocks are added progressively without considering the layout of the input trajectory or scene geometry, and may suffer from scarce training frames within individual blocks, especially when the trajectory returns to previously visited areas. In contrast, our framework determines basis positions and assigns a distance threshold around each basis, allowing nearby frames to be modeled together and thus avoiding this issue. See supplementary materials for additional results demonstrating the effect of our method under varying numbers of bases.

5. Conclusion

In this work, we propose scene-adaptive strategies to allocate basis using correlated information of geometry and camera trajectories to fully leverage limited resources. From the preprocessed geometric scaffold, we find optimal positions of bases to represent large-scale indoor scenes. We further regularize geometries that are unconstrained, using scene-aware virtual views and geometric priors. Through various experiments, we have verified that our framework significantly enhances baselines for challenging scenarios including extrapolation settings. Moreover, we have demonstrated the result for varying numbers of bases, where we could represent scenes with fewer bases while maintaining reconstruction quality comparable to the original implementations.

Although our approach shows performance improvements in general indoor environments, our framework does not account for view-dependent reflectance and may create artifacts in regions with complex lighting or strong reflectance. Also, our results degrade in regions with inevitable errors in geometric scaffold from MonoSDF [52], such as windows. Scaling our work to in-the-wild scenarios with complex appearance and lighting changes would be an interesting future work.

References

- [1] Jonathan T. Barron, Ben Mildenhall, Dor Verbin, Pratul P. Srinivasan, and Peter Hedman. Mip-nerf 360: Unbounded anti-aliased neural radiance fields. *CVPR*, 2022. 1, 4, 5, 6
- [2] Jonathan T. Barron, Ben Mildenhall, Dor Verbin, Pratul P. Srinivasan, and Peter Hedman. Zip-nerf: Anti-aliased grid-based neural radiance fields. *ICCV*, 2023. 2, 5, 6, 7, 8, 12, 14, 15, 16, 17, 18, 19, 21
- [3] Shariq Farooq Bhat, Reiner Birkl, Diana Wofk, Peter Wonka, and Matthias Müller. Zoedepth: Zero-shot transfer by combining relative and metric depth. *arXiv preprint arXiv:2302.12288*, 2023. 3
- [4] Wenjing Bian, Zirui Wang, Kejie Li, Jia-Wang Bian, and Victor Adrian Prisacariu. Nope-nerf: Optimising neural radiance field with no pose prior. In *Proceedings of the IEEE/CVF Conference on Computer Vision and Pattern Recognition*, pages 4160–4169, 2023. 3
- [5] Gary Bradski. The opencv library. *Dr. Dobbs' Journal: Software Tools for the Professional Programmer*, 25(11):120–123, 2000. 15
- [6] Anpei Chen, Zexiang Xu, Andreas Geiger, Jingyi Yu, and Hao Su. Tensorf: Tensorial radiance fields. In *European Conference on Computer Vision (ECCV)*, 2022. 4
- [7] Changwoon Choi, Sang Min Kim, and Young Min Kim. Balanced spherical grid for egocentric view synthesis. In *Proceedings of the IEEE/CVF Conference on Computer Vision and Pattern Recognition (CVPR)*, pages 16590–16599, 2023. 1
- [8] Dongyoung Choi, Hyeonjoong Jang, and Min H. Kim. Omnilocalrf: Omnidirectional local radiance fields from dynamic videos. In *IEEE Conference on Computer Vision and Pattern Recognition (CVPR)*, 2024. 2, 4
- [9] Kangle Deng, Andrew Liu, Jun-Yan Zhu, and Deva Ramanan. Depth-supervised NeRF: Fewer views and faster training for free. In *Proceedings of the IEEE/CVF Conference on Computer Vision and Pattern Recognition (CVPR)*, 2022. 2, 3
- [10] Ainaz Eftekhari, Alexander Sax, Jitendra Malik, and Amir Zamir. Omnidata: A scalable pipeline for making multi-task mid-level vision datasets from 3d scans. In *Proceedings of the IEEE/CVF International Conference on Computer Vision*, pages 10786–10796, 2021. 15, 16
- [11] Thibaud Ehret, Roger Marí, and Gabriele Facciolo. A generic and flexible regularization framework for nerfs. In *Proceedings of the IEEE/CVF Winter Conference on Applications of Computer Vision (WACV)*, pages 3088–3097, 2024. 15
- [12] Sara Fridovich-Keil, Alex Yu, Matthew Tancik, Qinhong Chen, Benjamin Recht, and Angjoo Kanazawa. Plenoxels: Radiance fields without neural networks. In *CVPR*, 2022. 1, 2, 16
- [13] Guangcong, Zhaoxi Chen, Chen Change Loy, and Ziwei Liu. Sparsenerf: Distilling depth ranking for few-shot novel view synthesis. *IEEE/CVF International Conference on Computer Vision (ICCV)*, 2023. 2, 3, 6, 15
- [14] Haoyu Guo, Sida Peng, Haotong Lin, Qianqian Wang, Guofeng Zhang, Hujun Bao, and Xiaowei Zhou. Neural 3d scene reconstruction with the manhattan-world assumption. In *CVPR*, 2022. 3
- [15] Bernhard Kerbl, Georgios Kopanas, Thomas Leimkühler, and George Drettakis. 3d gaussian splatting for real-time radiance field rendering. *ACM Transactions on Graphics*, 42(4), 2023. 6, 7, 16, 20
- [16] Bernhard Kerbl, Andreas Meuleman, Georgios Kopanas, Michael Wimmer, Alexandre Lanvin, and George Drettakis. A hierarchical 3d gaussian representation for real-time rendering of very large datasets. *ACM Transactions on Graphics*, 43(4), 2024. 6, 7, 16, 17
- [17] Arno Knapitsch, Jaesik Park, Qian-Yi Zhou, and Vladlen Koltun. Tanks and temples: Benchmarking large-scale scene reconstruction. *ACM Transactions on Graphics*, 36(4), 2017. 16
- [18] Georgios Kopanas and George Drettakis. Improving NeRF Quality by Progressive Camera Placement for Free-Viewpoint Navigation. In *Vision, Modeling, and Visualization*. The Eurographics Association, 2023. 2, 14
- [19] Jiahe Li, Jiawei Zhang, Xiao Bai, Jin Zheng, Xin Ning, Jun Zhou, and Lin Gu. Dngaussian: Optimizing sparse-view 3d gaussian radiance fields with global-local depth normalization. *arXiv preprint arXiv:2403.06912*, 2024. 6, 7, 16
- [20] Ruilong Li, Sanja Fidler, Angjoo Kanazawa, and Francis Williams. NeRF-XL: Scaling nerfs with multiple GPUs. In *European Conference on Computer Vision (ECCV)*, 2024. 2, 4
- [21] Yiyi Liao, Jun Xie, and Andreas Geiger. KITTI-360: A novel dataset and benchmarks for urban scene understanding in 2d and 3d. *Pattern Analysis and Machine Intelligence (PAMI)*, 2022. 17
- [22] Lingjie Liu, Jiatao Gu, Kyaw Zaw Lin, Tat-Seng Chua, and Christian Theobalt. Neural sparse voxel fields. *NeurIPS*, 2020. 2
- [23] William E. Lorensen and Harvey E. Cline. Marching cubes: A high resolution 3d surface construction algorithm. In *Proceedings of the 14th Annual Conference on Computer Graphics and Interactive Techniques*, page 163–169, New York, NY, USA, 1987. Association for Computing Machinery. 4
- [24] Julien N. P. Martel, David B. Lindell, Connor Z. Lin, Eric R. Chan, Marco Monteiro, and Gordon Wetzstein. Acorn: Adaptive coordinate networks for neural scene representation. *ACM Trans. Graph. (SIGGRAPH)*, 40(4), 2021. 2
- [25] Andreas Meuleman, Yu-Lun Liu, Chen Gao, Jia-Bin Huang, Changil Kim, Min H. Kim, and Johannes Kopf. Progressively optimized local radiance fields for robust view synthesis. In *CVPR*, 2023. 2, 4, 6, 7, 8, 16, 17, 21
- [26] Ben Mildenhall, Pratul P. Srinivasan, Rodrigo Ortiz-Cayon, Nima Khademi Kalantari, Ravi Ramamoorthi, Ren Ng, and Abhishek Kar. Local light field fusion: Practical view synthesis with prescriptive sampling guidelines. *ACM Transactions on Graphics (TOG)*, 2019. 6
- [27] Ben Mildenhall, Pratul P. Srinivasan, Matthew Tancik, Jonathan T. Barron, Ravi Ramamoorthi, and Ren Ng. Nerf:

- Representing scenes as neural radiance fields for view synthesis. In *ECCV*, 2020. 1, 6
- [28] Thomas Müller, Alex Evans, Christoph Schied, and Alexander Keller. Instant neural graphics primitives with a multiresolution hash encoding. *ACM Trans. Graph.*, 41(4):102:1–102:15, 2022. 1, 5
- [29] Michael Niemeyer, Jonathan T. Barron, Ben Mildenhall, Mehdi S. M. Sajjadi, Andreas Geiger, and Noha Radwan. Regnerf: Regularizing neural radiance fields for view synthesis from sparse inputs. In *Proc. IEEE Conf. on Computer Vision and Pattern Recognition (CVPR)*, 2022. 2, 8, 15
- [30] Xuran Pan, Zihang Lai, Shiji Song, and Gao Huang. Activenerf: Learning where to see with uncertainty estimation. In *Computer Vision–ECCV 2022: 17th European Conference, Tel Aviv, Israel, October 23–27, 2022, Proceedings, Part XXXIII*, pages 230–246. Springer, 2022. 2, 14
- [31] René Ranftl, Alexey Bochkovskiy, and Vladlen Koltun. Vision transformers for dense prediction. *ICCV*, 2021. 3, 8, 16
- [32] René Ranftl, Katrin Lasinger, David Hafner, Konrad Schindler, and Vladlen Koltun. Towards robust monocular depth estimation: Mixing datasets for zero-shot cross-dataset transfer. *IEEE Transactions on Pattern Analysis and Machine Intelligence*, 44(3), 2022. 3, 16
- [33] Barbara Roessle, Jonathan T. Barron, Ben Mildenhall, Pratul P. Srinivasan, and Matthias Nießner. Dense depth priors for neural radiance fields from sparse input views. In *Proceedings of the IEEE/CVF Conference on Computer Vision and Pattern Recognition (CVPR)*, 2022. 2, 3
- [34] Sara Fridovich-Keil and Giacomo Meanti, Frederik Rahbæk Warburg, Benjamin Recht, and Angjoo Kanazawa. K-planes: Explicit radiance fields in space, time, and appearance. In *CVPR*, 2023. 1
- [35] Johannes Lutz Schönberger and Jan-Michael Frahm. Structure-from-motion revisited. In *Conference on Computer Vision and Pattern Recognition (CVPR)*, 2016. 1, 3, 15
- [36] Nagabhushan Somraj and Rajiv Soundararajan. ViP-NeRF: Visibility prior for sparse input neural radiance fields. *ACM Trans. Graph.*, 2023. 2
- [37] Cheng Sun, Min Sun, and Hwann-Tzong Chen. Direct voxel grid optimization: Super-fast convergence for radiance fields reconstruction. In *CVPR*, 2022. 1
- [38] Matthew Tancik, Vincent Casser, Xinchen Yan, Sabeek Pradhan, Ben Mildenhall, Pratul P. Srinivasan, Jonathan T. Barron, and Henrik Kretzschmar. Block-nerf: Scalable large scene neural view synthesis. *arXiv*, 2022. 2, 4
- [39] Matthew Tancik, Ethan Weber, Evonne Ng, Ruilong Li, Brent Yi, Justin Kerr, Terrance Wang, Alexander Kristoffersen, Jake Austin, Kamyar Salahi, Abhik Ahuja, David McAllister, and Angjoo Kanazawa. Nerfstudio: A modular framework for neural radiance field development. In *ACM SIGGRAPH 2023 Conference Proceedings*, 2023. 5, 6, 7, 16, 20
- [40] Haithem Turki, Deva Ramanan, and Mahadev Satyanarayanan. Mega-nerf: Scalable construction of large-scale nerfs for virtual fly-throughs. In *Proceedings of the IEEE/CVF Conference on Computer Vision and Pattern Recognition (CVPR)*, pages 12922–12931, 2022. 2, 4, 6, 7, 16, 21
- [41] Mikaela Angelina Uy, Ricardo Martin-Brualla, Leonidas Guibas, and Ke Li. Scade: Nerfs from space carving with ambiguity-aware depth estimates. In *Conference on Computer Vision and Pattern Recognition (CVPR)*, 2023. 2, 3
- [42] Peng Wang, Lingjie Liu, Yuan Liu, Christian Theobalt, Taku Komura, and Wenping Wang. Neus: Learning neural implicit surfaces by volume rendering for multi-view reconstruction. *arXiv preprint arXiv:2106.10689*, 2021. 3
- [43] Jamie Wynn and Daniyar Turmukhambetov. DiffusioNeRF: Regularizing Neural Radiance Fields with Denoising Diffusion Models. In *CVPR*, 2023. 8
- [44] Wenhui Xiao, Rodrigo Santa Cruz, David Ahméd-Aristizabal, Olivier Salvado, Clinton Fookes, and Leo Lebrat. Nerf director: Revisiting view selection in neural volume rendering. In *Proceedings of the IEEE Conference on Computer Vision and Pattern Recognition (CVPR)*, 2024. 2, 5, 14
- [45] Shangjie Xue, Jesse Dill, Pranay Mathur, Frank Dellaert, Panagiotis Tsotra, and Danfei Xu. Neural visibility field for uncertainty-driven active mapping. In *Proceedings of the IEEE/CVF Conference on Computer Vision and Pattern Recognition*, pages 18122–18132, 2024. 2
- [46] Chen Yang, Peihao Li, Zanwei Zhou, Shanxin Yuan, Bingbing Liu, Xiaokang Yang, Weichao Qiu, and Wei Shen. Nerfvs: Neural radiance fields for free view synthesis via geometry scaffolds. In *Proceedings of the IEEE/CVF Conference on Computer Vision and Pattern Recognition*, pages 16549–16558, 2023. 3, 5
- [47] Lior Yariv, Jiatao Gu, Yoni Kasten, and Yaron Lipman. Volume rendering of neural implicit surfaces. In *Thirty-Fifth Conference on Neural Information Processing Systems*, 2021. 3
- [48] Chandan Yeshwanth, Yueh-Cheng Liu, Matthias Nießner, and Angela Dai. Scannet++: A high-fidelity dataset of 3d indoor scenes. In *Proceedings of the International Conference on Computer Vision (ICCV)*, 2023. 2, 5, 6, 8, 12, 13, 14, 15, 17, 18, 19, 20
- [49] Zinuo You, Andreas Geiger, and Anpei Chen. Nelf-pro: Neural light field probes for multi-scale novel view synthesis. In *Conference on Computer Vision and Pattern Recognition (CVPR)*, 2024. 2, 4, 5, 6, 7, 8, 12, 14, 16, 17, 20, 21
- [50] Alex Yu, Ruilong Li, Matthew Tancik, Hao Li, Ren Ng, and Angjoo Kanazawa. PlenOctrees for real-time rendering of neural radiance fields. In *ICCV*, 2021. 1, 2
- [51] Zehao Yu, Anpei Chen, Bozidar Antic, Songyou Peng, Apratim Bhattacharyya, Michael Niemeyer, Siyu Tang, Torsten Sattler, and Andreas Geiger. Sdfstudio: A unified framework for surface reconstruction, 2022. 5, 15
- [52] Zehao Yu, Songyou Peng, Michael Niemeyer, Torsten Sattler, and Andreas Geiger. Monosdf: Exploring monocular geometric cues for neural implicit surface reconstruction. *Advances in Neural Information Processing Systems (NeurIPS)*, 2022. 3, 5, 6, 7, 8, 15, 16, 17

- [53] Kai Zhang, Gernot Riegler, Noah Snaveley, and Vladlen Koltun. Nerf++: Analyzing and improving neural radiance fields. *arXiv preprint arXiv:2010.07492*, 2020. [1](#)
- [54] Qian-Yi Zhou, Jaesik Park, and Vladlen Koltun. Open3D: A modern library for 3D data processing. *arXiv:1801.09847*, 2018. [15](#)
- [55] Zehao Zhu, Zhiwen Fan, Yifan Jiang, and Zhangyang Wang. Fsgs: Real-time few-shot view synthesis using gaussian splatting. In *European conference on computer vision*, pages 145–163. Springer, 2024. [6](#), [7](#), [16](#), [17](#)

Geometry-Aware Scene Configurations for Novel View Synthesis

Supplementary Material

A. Basis Placement Optimization

A.1. Algorithms and Optimization Results

In this section, we demonstrate the results of the obtained coverage weights and corresponding basis positions. We outline the detailed process of obtaining a coverage weight map in Algorithm 1. To obtain the coverage weight for each point in the geometry scaffold, we accumulate the observation statistics of all training cameras, with the consideration of the visibility of each point. We calculate visibility by projecting the points sampled from the geometry scaffold into the camera frustum, and discard those whose orientations face away from the camera according to the scaffold normals. Additionally, we leverage depth map which is directly obtained from geometry scaffold to further filter out points located behind the depth surface. Once the coverage weight map is constructed, it serves as an input to the basis optimization process as described in Algorithm 2.

We illustrate coverage weights and optimized basis positions in Fig. 2 for two example scenes, each from ScanNet++ [48] and Zip-NeRF [2] datasets. To help the understanding of our optimization scheme, we optimized eight basis positions, while 64 and 128 bases are used in real experiments for NeLF-pro [49] variants. We visualize the initial bases positions, with training and evaluation cameras in Fig. 2 (a), while the coverage weight map and optimized

Algorithm 1: Coverage weight calculation

Input : Geometry scaffold \mathcal{G} , Cameras \mathcal{C}
Output : Coverage weight w_i

Initialize:
 $\mathbf{x}_i, \hat{\mathbf{n}}_i \leftarrow$ point, normal from \mathcal{G}
 $\mathbf{c}_k, \mathcal{M}_k \leftarrow$ camera center, proj matrix from \mathcal{C}
 $\mathcal{D}_k \leftarrow$ Depth map from \mathcal{G}
 $w_i \leftarrow 0$

foreach $\{\mathbf{c}_k, \mathcal{M}_k\} \in \mathcal{C}$ **do**

- $\text{Vis}(\mathbf{c}_k \rightarrow \mathbf{x}_i) \leftarrow 1$
- $(u_i, v_i, z_i) \leftarrow$ project \mathbf{x}_i with \mathcal{M}_k
- if** $|u_i| > 1$ **or** $z_i < 0$ **then**

 - $\text{Vis}(\mathbf{c}_k \rightarrow \mathbf{x}_i) \leftarrow 0$

- if** $z_i - \mathcal{D}_k > \epsilon$ **then**

 - $\text{Vis}(\mathbf{c}_k \rightarrow \mathbf{x}_i) \leftarrow 0$

- if** $\hat{\mathbf{n}}_i \cdot (\mathbf{c}_k - \mathbf{x}_i) < 0$ **then**

 - $\text{Vis}(\mathbf{c}_k \rightarrow \mathbf{x}_i) \leftarrow 0$

$w_i \leftarrow w_i + \frac{\hat{\mathbf{n}}_i \cdot (\mathbf{c}_k - \mathbf{x}_i)}{\|\mathbf{c}_k - \mathbf{x}_i\|^2} \cdot \text{Vis}(\mathbf{c}_k \rightarrow \mathbf{x}_i)$

return w_i

Algorithm 2: Basis placement optimization

Input : Point set $\mathcal{X} = \{\mathbf{x}_i | \mathbf{x}_i \in \mathbb{R}^3\}_{i=1}^B$,
Normal set $\mathcal{N} = \{\hat{\mathbf{n}}_i | \hat{\mathbf{n}}_i \in \mathbb{R}^3\}_{i=1}^B$,
Coverage weight set $\mathcal{W} = \{w_i | w_i \in \mathbb{R}\}_{i=1}^B$

Output : Optimized basis positions
 $\mathcal{P} = \{\mathbf{p}_j | \mathbf{p}_j \in \mathbb{R}^3\}_{j=1}^{N_p}$

Initialize:
 $\mathcal{P} \leftarrow$ Initial basis positions using FPS algorithm

for $\text{iter} = 1$ **to** maxiter **do**

- $\mathbf{p}_{\mathcal{C}(i)} \leftarrow \arg \min_{\mathbf{p}_j} \|\mathbf{p}_j - \mathbf{x}_i\| \quad \forall \mathbf{x}_i \in \mathcal{X}, \mathbf{p}_j \in \mathcal{P}$
- $\mathcal{L}_{\text{cov}} \leftarrow \sum_{i=1}^B w_i \left(\frac{\|\mathbf{p}_{\mathcal{C}(i)} - \mathbf{x}_i\|^3}{\hat{\mathbf{n}}_i \cdot (\mathbf{p}_{\mathcal{C}(i)} - \mathbf{x}_i) + \epsilon} \right)$
- $\mathbf{p}_{\mathcal{C}(i)} \leftarrow \mathbf{p}_{\mathcal{C}(i)} - \alpha \nabla_{\mathbf{p}_{\mathcal{C}(i)}} \mathcal{L}_{\text{cov}}$

return \mathcal{P}

bases positions are depicted in Fig. 2 (b). The basis positions are effectively drawn to regions with frequent measurements.

A.2. Analysis of Coverage Loss

The coverage loss \mathcal{L}_{cov} in Eq.(6) of our main manuscript is designed to ensure that the basis positions effectively accumulate the coverage while considering the geometry of the scene. In the coverage loss term, we can decompose the component multiplied by the coverage weight as follows:

$$\frac{\|\mathbf{p}_{\mathcal{C}(i)} - \mathbf{x}_i\|^3}{\hat{\mathbf{n}}_i \cdot (\mathbf{p}_{\mathcal{C}(i)} - \mathbf{x}_i) + \epsilon} = \frac{\|\mathbf{p}_{\mathcal{C}(i)} - \mathbf{x}_i\|^2}{\widehat{\hat{\mathbf{n}}_i \cdot (\mathbf{p}_{\mathcal{C}(i)} - \mathbf{x}_i)} + \tilde{\epsilon}}, \quad (11)$$

where $\widehat{(\mathbf{p}_{\mathcal{C}(i)} - \mathbf{x}_i)}$ denotes the normalized directional vector. The term $\|\mathbf{p}_{\mathcal{C}(i)} - \mathbf{x}_i\|$ in the numerator represents the Euclidean distance between a point \mathbf{x}_i and its closest basis position $\mathbf{p}_{\mathcal{C}(i)}$. The denominator $\widehat{\hat{\mathbf{n}}_i \cdot (\mathbf{p}_{\mathcal{C}(i)} - \mathbf{x}_i)} + \tilde{\epsilon}$ incorporates the normal vector $\hat{\mathbf{n}}_i$ at \mathbf{x}_i to enforce alignment between the basis position and the underlying surface geometry. Without the denominator, the loss would only encour-

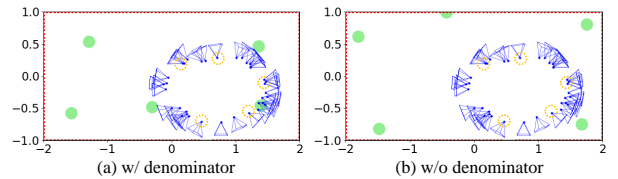


Figure 1. **2D toy examples of basis placement.** We evaluate basis placement using \mathcal{L}_{cov} (a) with and (b) without the denominator. Initial basis (circle outlines), optimized basis (solid green circles), and observation views (blue frustums) are visualized.

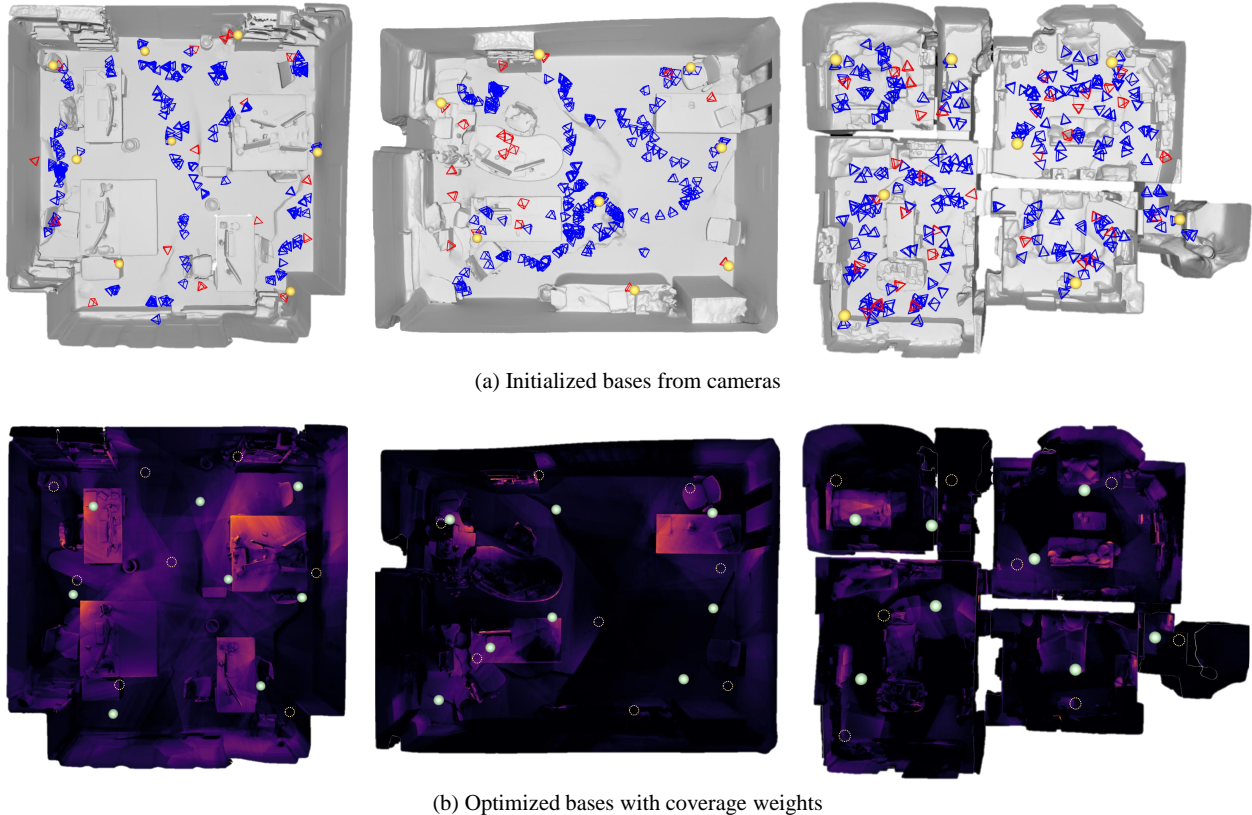


Figure 2. **Coverage weights and optimized basis positions.** (a) Given training (blue) and test (red) cameras, initial bases (yellow spheres) are obtained using FPS on cameras. (b) Optimized bases are distributed at balanced positions regarding the coverage weight. Initial bases locations are indicated with sphere outlines, while the optimized bases are solid spheres in a bright green color.

age closeness in Euclidean distance, disregarding the local surface orientation as illustrated in the 2D toy example of Fig. 1. The denominator ensures that the basis positions are not only close to the points but also aligned with the surface normal, resulting in more accurate placement within structured environments. The small term ϵ is added to the denominator to prevent numerical instability when the dot product $\hat{\mathbf{n}}_i \cdot (\mathbf{p}_{C(i)} - \mathbf{x}_i)$ approaches zero.

A.3. Ablation of Basis Placement

We conducted an ablation study to analyze the effect of basis placement strategies on reconstruction quality. Specifically, we compared three configurations: (1) uniform dis-

# Basis	4	8	16	32	64
trajectory	19.89	19.69	19.97	19.90	20.15
uniform	19.91	19.87	19.95	20.22	20.11
optimal (ours)	20.21	20.07	20.37	20.29	20.46

Table 1. **Ablation study for different basis placements.** PSNRs are reported for different number of bases.

tribution within the estimated geometric scaffold, (2) uniform placement along the camera trajectory, and (3) optimal placement based on scene geometry and observation statistics. These experiments were conducted across varying numbers of bases to assess consistency and performance under different representation budgets. We demonstrate the results using the ScanNet++ [48] e91722b5a3 scene in Tab. 1, clearly indicating that optimized placement consistently outperforms both uniform-in-geometry and trajectory-based strategies. These results highlight the importance of scene-adaptive placement for achieving efficient and expressive representations.

A.4. Perturbing Optimized Basis

To further understand the robustness of our optimized basis configuration, we explore how sensitive the system is to perturbations in placement. We conducted experiments to verify the effect of shifting bases from the optimized positions. Using the optimal set of bases positions, we have gradually added the random noise to the bases positions with varying noise scales from 0.1 to 1.5 and measured the PSNR of the rendering results compared to the validation

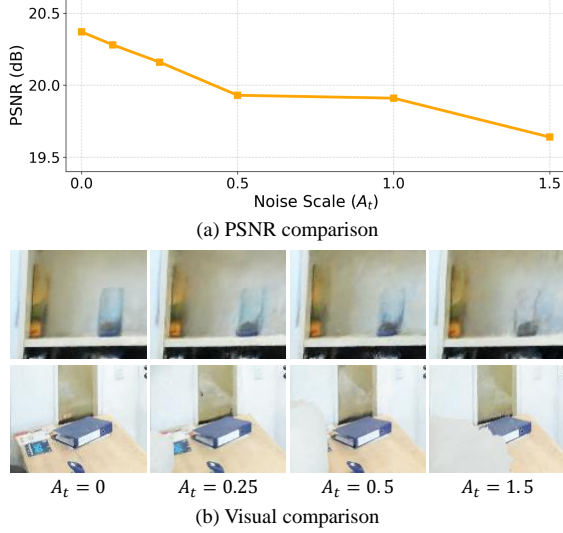


Figure 3. **Shifting optimized basis positions.** (a) PSNR comparisons with different levels of perturbation noise scales. (b) Enlargements of rendered images for visual comparison of sampled noise levels.

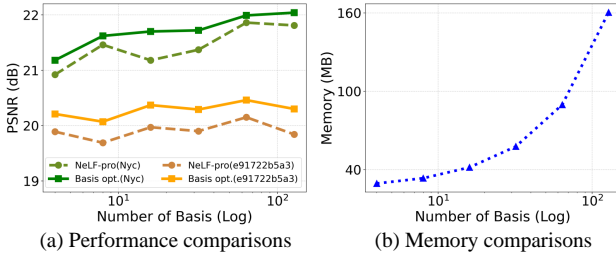


Figure 4. **Experiments for different number of bases.** (a) Performance comparisons and (b) memory comparisons are plotted.

set. To clearly analyze the effects of basis perturbation, we used neural lightfield probes, reducing the number of basis probes to 16, with 4 nearby probes contributing to rendering. We have tested on ScanNet++ [48] e91722b5a3 scene for this experiment. As the bases are perturbed, they deviate from the regions with the high-density training rays, hence making it difficult to model highly informative regions. The rendering quality degrades gradually as the basis placement perturb from the optimal as shown in Fig. 3.

A.5. Comparison for Varying Number of Bases

To isolate the impact of the basis placement, we evaluated PSNR performance with and without the basis placement under a varying number of neural lightfield probes. Different from the experiments conducted in Fig. 9 of the main manuscript, we removed the effects of our geometric regularization strategy. We set the number of bases within the range of 4 to 128, identical to those used in the previous experiment. For evaluation, we selected e91722b5a3 scene

from ScanNet++ [48] and NYC scene from Zip-NeRF [2] dataset. Additionally, we report the required memory for different numbers of bases to show the trade-off between performance and computational cost. As shown in Fig. 4 (a), our basis placement strategy consistently improves the performance of NeLF-Pro [49] across all tested basis numbers. While our framework uses the same memory as the NeLF-pro, the memory consumption scales with the number of bases. These results confirm that the optimal basis placement enhances reconstruction quality for different basis settings while remaining the number of parameter and memory usage unchanged.

B. Scene-Adaptive Geometric Regularization

B.1. Algorithms and Sampled Virtual Depths

In this section, we present a detailed process for sampling virtual depths in Algorithm 3. In addition, we serve several supplementary examples of depth maps rendered from virtual viewpoints, that were used in our experiments in Fig. 10. Unlike common next-best-view planning setups [18, 30, 44], we do not have images for candidate viewpoints. In other words, feature correspondences between candidate viewpoints were not prepared. Therefore, to calculate a scene similarity matrix \mathcal{A}_{v_s} in Sec. 3.3 of

Algorithm 3: Novel viewpoint sampling

Input : Geometry scaffold \mathcal{G} ,
Cameras $\mathcal{C} \in \mathbb{R}^{N_c \times 3 \times 4}$,
Feature points $\mathcal{X} = \{\mathbf{x}_i | \mathbf{x}_i \in \mathbb{R}^3\}_{i=1}^{N_{fp}}$
Output : Sampled cameras $\mathcal{S} = \{s_i | s_i \in \mathbb{R}^{3 \times 4}\}_{i=1}^n$
Initialize:
 $\mathcal{V} \leftarrow \{v_i | v_i \in \mathbb{R}^{3 \times 4}\}_{i=1}^N$ (random candidate cameras)
 $\mathcal{S} \leftarrow \mathcal{C}$
 $\mathcal{A}_{v_s} \in \mathbb{R}^{(N+N_c) \times (N+N_c)} \leftarrow 0$ // Similarity matrix
// Build similarity matrix
foreach $\mathbf{x}_i \in \mathcal{X}$ **do**
 $i_{\text{visible}} \leftarrow 0 \in \mathbb{R}^{(N+N_c) \times 1}$
 foreach $(j, c) \in \text{enumerate}(\mathcal{V} \cup \mathcal{S})$ **do**
 if $\text{VisibilityCheck}(\mathbf{x}_i, c)$ **then**
 $i_{\text{visible}}[j] \leftarrow 1$
 foreach $(i_p, i_q) \in \text{Pairs}(i_{\text{visible}})$ **do**
 $\mathcal{A}_{v_s}[i_p, i_q] \leftarrow \mathcal{A}_{v_s}[i_p, i_q] + 1$
// Sample virtual viewpoints
while $|\mathcal{S}| < n$ **do**
 $c_v, c_s \leftarrow$ positions of v, s
 $i_v, i_s \leftarrow$ indices of v, s
 $d_{\text{euc}} \leftarrow \|c_v - c_s\|$
 $d_{\text{feat}} \leftarrow 1 - \mathcal{A}_{v_s}[i_v, i_s]$
 $v^* \leftarrow \arg \max_{v \in \mathcal{V} \setminus \mathcal{S}} \min_{s \in \mathcal{S}} (d_{\text{euc}} + \kappa d_{\text{feat}})$
 $\mathcal{S} \leftarrow \mathcal{S} \cup \{v^*\}$
return \mathcal{S}

the main paper, we utilized the triangulated feature points from COLMAP [35]. For the given 3D feature points and cameras, we computed the occlusion on camera rays using the RaycastingScene class in Open3D [54]. If the points are visible in multiple cameras, we update only the elements of the similarity matrix corresponding to those camera indices. Depth maps sampled from two scenes of the ScanNet++ dataset are illustrated in Fig. 10.

B.2. Robustness to Inaccurate Geometry

As we are using geometry scaffolds from the implicit surface reconstruction model, the predictions could be inaccurate. To test the robustness of inaccurate geometry, we examine the performance of our method when the geometric scaffolds are contaminated. For these experiments, we directly use the ground truth geometry to simulate the scaffold and apply different degrees of noise to observe the dependence of the model’s effectiveness on the accuracy of geometry prediction. For ScanNet++ [48] scenes, ground truth scanned meshes are given. We rendered depth using the mesh for ef69d58016 scene and used it as the ground truth depth. We have perturbed the ground truth depth by adding Gaussian blur and random noise with different scales as shown in Fig. 5. Note that the RGB image in Fig. 5 (a) is only given for visualization and not used for our experiments. We report the performance comparisons with different noise levels in Tab. 2. Even when we used some severely noised depth inputs, the reconstruction still shows improved results compared to the case without depth supervision.

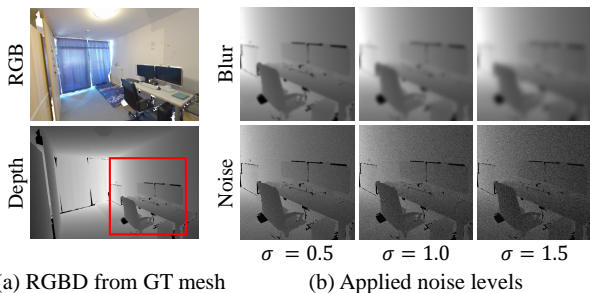


Figure 5. **Examples of inaccurate geometries.** (a) Rendered RGBD from GT mesh and (b) example depth inputs with different noise levels.

Blur	PSNR	Noise	PSNR	Reference	PSNR
$\sigma = 0.25$	27.61	$\sigma = 0.25$	27.61	NeLF-pro	26.83
$\sigma = 0.5$	27.49	$\sigma = 0.5$	27.52	Ours w/o depth	26.96
$\sigma = 1.0$	27.40	$\sigma = 1.0$	27.27	Ours w/ GT depth ($\sigma = 0$)	27.67
$\sigma = 1.5$	27.21	$\sigma = 1.5$	27.23	Ours w/ MonoSDF depth	27.20

Table 2. **Performance comparisons for experiments using inaccurate depth inputs.**

Method	ScanNet++			Zip-NeRF		
	PSNR \uparrow	SSIM \uparrow	LPIPS \downarrow	PSNR \uparrow	SSIM \uparrow	LPIPS \downarrow
SparseNeRF	21.75	0.808	0.332	20.64	0.710	0.486
RegNeRF	18.39	0.728	0.482	18.26	0.637	0.567
DiffNeRF	18.57	0.736	0.473	18.54	0.649	0.544
Ours	22.52	0.814	0.329	23.89	0.762	0.400

Table 3. **Comparison for different geometric regularizations.**

B.3. Comparisons for Depth Regularization

We conducted several experiments by comparing the geometric regularization strategy on controlled setting to verify the effectiveness of our geometry regularization strategy. We fixed all other components and compared the regularization strategy. We compared our depth regularization strategy to regularization methods in RegNeRF [29], DiffNeRF [11] and SparseNeRF [13] in Table 3. As our depth maps are noisy and we use dense observations, those regularization don’t increase the performance in our cases. The robust depth loss with our scene-aware regularization using the correlated information of the geometry and camera demonstrates the strongest performance increase.

C. Implementation Details

C.1. Datasets

We used ScanNet++ [48] and Zip-NeRF dataset [2] to evaluate our framework.

(1) ScanNet++: We use images captured from DSLR cameras and undistorted them using the OpenCV python package [5]. Test sets are predefined and include both interpolation and extrapolation settings. We selected six scenes for evaluation: [785E7504B9, EF69D58016, BB87C292AD, 0D2EE665BE, E91722B5A3, 281BA69AF1].

(2) Zip-NeRF dataset: We sample roughly 300 indoor frames to evaluate multi-room indoor scenarios. Test views are taken from every eight frames among sampled sequences. Among the entire dataset, four undistorted datasets were selected for evaluation: [BERLIN, NYC, ALAMEDA, LONDON].

C.2. Obtaining Geometric Scaffold

For geometric scaffold, we employed MonoSDF [52] included in the SDFStudio project [51]. Among model options introduced in the original MonoSDF, we used multi-resolution feature grids with an MLP. While training neural implicit surface models, we leverage ground truth depths and normals obtained from Omnidata [10] for geometric regularizations. For several scenes that have severe lighting changes, we apply learnable per-frame appearance embeddings. We train every model for 200000 steps.

C.3. Radiance Fields Optimization

Multiple NeRF blocks optimization In addition to the multiple NeRF block optimization details introduced in Sec. 3.2 of the main paper, we have tuned several parameters used in LocalRF [25]. We first removed Laplacian weights that were multiplied in the original implementation. As we optimize radiance fields without camera pose optimization, simple RGB supervision without Laplacian weighting worked better. We further remove flow loss and per-frame progressive optimization for all experiments, as those produce worse results for our dataset. Next, we do not set the maximum number of frames per NeRF block which is set to 100 frames for original LocalRF implementation. In other words, we only consider drifts when allocating new NeRF blocks. We finally adjusted the scene scale to allocate the number of blocks between 6 and 10 blocks, and increased iterations per frame from 600 to 1000 for experiments to ensure convergence.

Neural lightfield probe optimization As mentioned in Sec 3.2 of the main paper, we sort per ray sample to calculate nearby lightfield probes. Unlike FPS-based probe allocation, simply calculating nearby probes based on camera positions does not ensure full usage of probes. Several probes are not selected if the probe is located near the surface region far from the camera position. Hence, to fully utilize given resources, determining nearby probes per each ray sample is important. With PyTorch sorting implementation, only about an additional 0.3ms per optimization step is required for this modification on the NVIDIA GeForce RTX 4090 GPU. While optimizing NeLF-pro models with novel view regularization, we sample additional rays from the novel viewpoint, so that the number of rays used in RGB supervision is maintained identical. Similar to the case training MonoSDF, we jointly train the model with learnable appearance embeddings if large exposure variations exist. All of the models, including the baselines, are trained for a total of 30000 steps. Here, we verify our method using neural feature grids with NeLF-pro formulation. We used 64 basis and 3 core probes to model the ScanNet++ scenes while 16 near basis and 3 core probes contribute to volume rendering. For Zip-NeRF dataset, 128 basis and 3 core probes are used, while the same number of probes that were used in the ScanNet++ experiment contribute to image rendering.

C.4. Hyperparameters

After obtaining geometry scaffolds, 8192 surface points were batchified, each contributing to the position updates of their nearest bases. We used an ADAM optimizer with an initial learning rate of 0.0016. A standard exponential scheduling strategy was used similar to that of Plenoxels and 3DGS [12, 15]. During geometric regularization, we use $\gamma = 0.1$ in Eq. (7) of the main paper for all exper-

iments. To regularize geometry using unobserved viewpoint, we sample $N = 5000$ views for candidates and select 100 views in addition to the initial training views. We use $\kappa = 0.1$ for view distance calculation in Eq. (9) of the main paper. In Eq. (10) of the main paper, we used $\lambda_{\text{robust}} = 0.005$ for NeLF-pro and $\lambda_{\text{robust}} = 0.01$ for LocalRF experiments. To determine these values, we searched λ_{robust} for values between [0.001, 0.2], to maximize the validation image quality metrics. We set λ_{robust} within a specific range ([0.001, 0.01] for NeLF-pro and [0.005, 0.02] for LocalRF), where image quality does not change significantly. For λ_{reg} , we follow the weights that were used in the original implementations as L_{reg} is not our contribution.

D. Baseline Details

Although we have mentioned several details of baselines in Sec. 4.1 of the main paper, our different configurations for multiple baselines could lead to confusion for readers. Hence, we summarized each training configuration in Tab. 4. We compared all the baselines and our methods in terms of training iterations, depth inputs for regularizations, and basis type. We follow iterations of the official implementation except for NeLF-pro and LocalRF variants.

E. Scalability Analysis

E.1. Outdoor Experiments

While the proposed geometric adaptation demonstrates superior performance in non-convex indoor layouts, the same principle can also be applied to outdoor environments. We demonstrate the results of the outdoor experiments using Scuol [49] and Tanks and Temples [17] dataset (Barn scene)

Method	Iterations	Depth input	Basis type
MonoSDF [52]	200K	Omnidata [10]	✗
NeRFacto [39]	30K	✗	✗
NeRFacto [39]-Big	60K	✗	✗
NeRFacto [39]-Huge	60K	✗	✗
Depth-NeRFacto [39]	30K	Geo. scaffold	✗
Zip-NeRF [2]	30K	✗	✗
3DGS [15]	30K	✗	✗
FSGS [55]	30K	MiDaS [32]	✗
DNGaussian [19]	30K	DPT [32]	✗
Mega-NeRF [40]	200K / basis	✗	NeRF block
Hierarchical-3DGS [16]	30K	DPT [31]	Chunk
NeLF-pro [49]	30K	✗	LF probe
NeLF-pro [49] + Ours	30K	Geo. scaffold	LF probe
LocalRF [25]	1K / image	DPT [31]	NeRF block
LocalRF [25] + Ours	1K / image	Geo. scaffold	NeRF block

Table 4. **Baseline configurations.** The table is separated based on the number of bases, where methods in lower rows leverage multiple bases. For cases where depth regularization is not used, we filled those cells with ✗. Similarly, for single-basis representations, we filled those cells with ✗.



Figure 6. **Qualitative comparisons in Scuol dataset.** We compared our framework to NeLF-pro and Depth-NeRFacto.

	Tanks (Barn)			Scuol		
	PSNR \uparrow	SSIM \uparrow	LPIPS \downarrow	PSNR \uparrow	SSIM \uparrow	LPIPS \downarrow
Depth-NeRFacto	17.04	0.634	0.571	18.21	0.676	0.471
NeLF-pro	21.12	0.652	0.556	25.44	0.779	0.3
NeLF-pro+Ours	21.88	0.654	0.523	25.73	0.781	0.236
LocalRF	21.33	0.706	0.566	22.54	0.776	0.418
LocalRF+Ours	22.20	0.711	0.511	23.01	0.780	0.359

Table 5. **Quantitative evaluation on outdoor datasets.** Metrics are reported as PSNR (\uparrow), SSIM (\uparrow), and LPIPS (\downarrow).

Scene scale	Single-Room	Multi-Rooms	Outdoor	Town-scale
NeLF-pro	22.58	22.44	21.12	25.44
NeLF-pro+Ours	23.06	23.08	21.88	25.73
LocalRF	Non-sequential	21.39	21.33	22.54
LocalRF+Ours	Non-sequential	23.02	22.20	23.01

Table 6. **Evaluation for different scales with baselines.**

in Tab. 5. MonoSDF [52] struggles with sky and background regions in outdoor environments, which could degrade the optimization of the basis and geometric regularization. To test our method on outdoor scenarios, we manually extracted the bounding box of the valid mesh and optimized the basis placement. We further reduced outlier weights for outside regions in Eq. (7) of the main paper, ignoring the far-away objects. While we demonstrate improved results for selected scenes, scenes with severely low mesh quality (e.g., KITTI-360 [21]) face limitations when applying indoor-oriented geometry scaffolds to the unconstrained outdoor environments. Future work could explore handling complex outdoor scenes with distant or ambiguous geometry.

E.2. Evaluation for Different Scales

We demonstrate scalability analysis with additional results in Tab. 6, where scenes are categorized as single-room, multi-room, outdoor, and town scale. For outdoor and town scale scene, we reported PSNRs for the BARN scene and Scuol dataset, which were demonstrated in Fig. 6 and Tab. 5. The scalability analysis shows that our method can consistently handle the scenes as scale increases. Real-time rendering is out of the scope of this work, as we follow the rendering speed of NeLF-pro [49] and LocalRF [25].

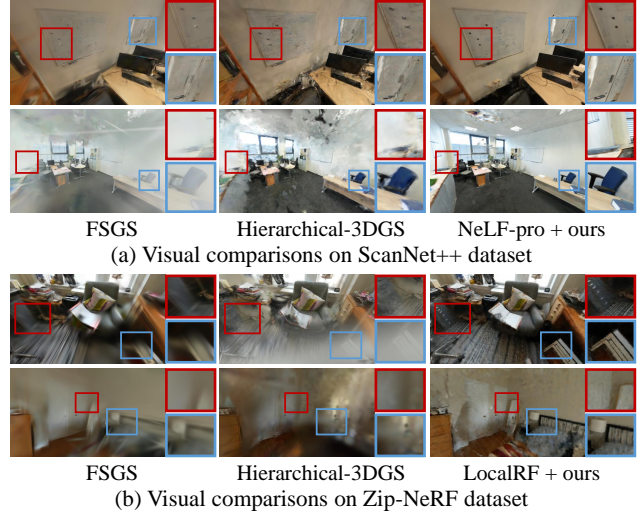


Figure 7. **Comparisons to SOTA 3DGS algorithms.** We compared our frameworks using both (a) ScanNet++ and (b) Zip-NeRF datasets.

F. Additional Comparisons

Comparison to SOTA 3DGS algorithms We additionally conducted visual comparisons of our methods with SOTA 3DGS baselines. We compared our methods to FSGS [55] and Hierarchical-3DGS [16] as in the main manuscript. For NeLF-pro [49] and LocalRF [25] variants, we evaluated them on ScanNet++ [48] and Zip-NeRF [2] datasets, respectively. As shown in visual comparisons in Fig. 7, recent SOTA 3DGS algorithms still exhibit significant overfitting to training views and fail to handle our experimental settings properly.

Limitation We demonstrate some examples of the inaccurate reconstruction around the window areas in Fig. 8. The use of the indoor geometry scaffold introduces errors in window regions, since the scaffold does not correctly reconstruct the outdoor areas. Future work may explore accurately reconstructing the surfaces with glossy materials or transparency.

Measurement of standard deviations To verify that our framework outperforms baselines, we have measured standard deviation using 5 randomly initialized seeds. Among the baselines, we visualize the error bars of NeLF-pro and 3DGS in Fig. 9. In addition, we have included a comparison to ablation studies, which shows the robustness of each component on performance enhancement.

Effects of each component To show the effect of the components of our framework, we demonstrate visualizations for the ablation studies in Fig. 11 and Fig. 12. We



Figure 8. **Examples of limitation.**

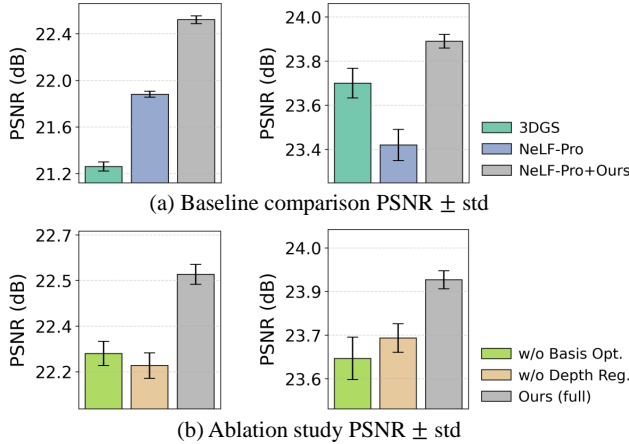
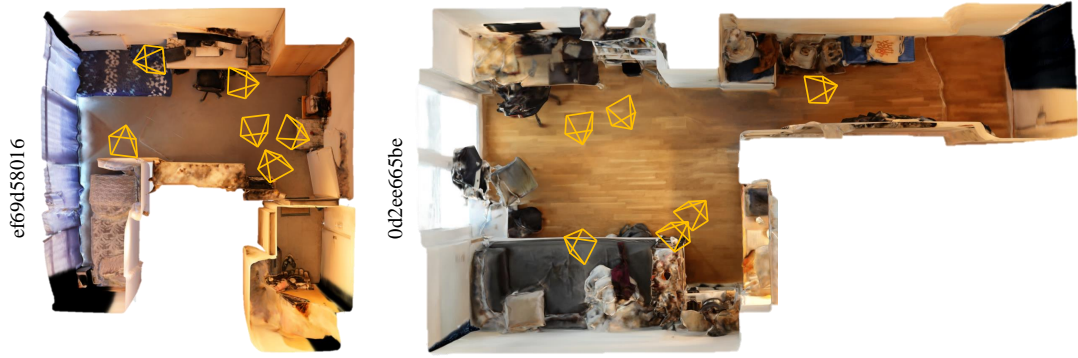


Figure 9. **Error bars for our experiments.** We compared (a) baselines and (b) ablation studies on ScanNet++ (left) and Zip-NeRF (right) dataset.

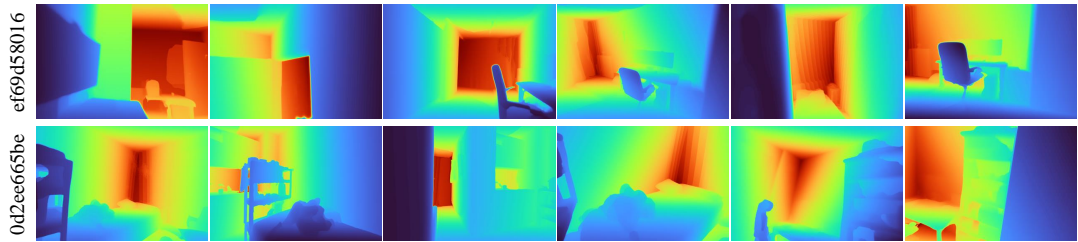
tested NeLF-pro variants on ScanNet++ dataset and LocalRF variants on Zip-NeRF dataset, respectively. As illustrated in both figures, while optimal basis placement helps reduce blurry artifacts, our geometric regularization with virtual viewpoints further enhances stability of the reconstruction. In both figures, we follow the notations that were used in the main paper ; ①: basis optimization, ②: robust depth loss for training views, ③: novel view depth regularization, and ④: random unobserved view depth regularization.

Qualitative results We present additional qualitative results for both ScanNet++ [48] and Zip-NeRF [2] datasets in Fig. 13 and Fig. 14. All six scenes from ScanNet++ and four scenes from the Zip-NeRF dataset are illustrated. By incorporating our optimal basis placements and geometric regularization into prior scene representations, we achieve a notable reduction of artifacts, particularly in textureless or under-constrained regions where traditional NeRF-based methods often struggle. Compared to the baselines, our method produces cleaner geometry, and more photorealistic synthesis under novel viewpoints. This improvement highlights the effectiveness of our method in reducing ambigu-

ity and enabling stable reconstructions across diverse scene layouts.



(a) Geometry scaffold with sampled viewpoints



(b) Depth maps from virtual viewpoints

Figure 10. Sampled virtual depths from ScanNet++ [48] dataset

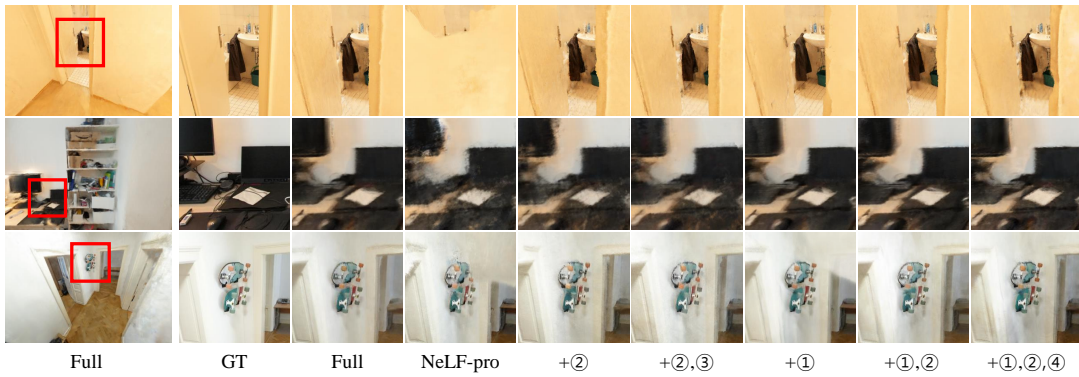


Figure 11. Qualitative results for ablation study on ScanNet++ [48] dataset.

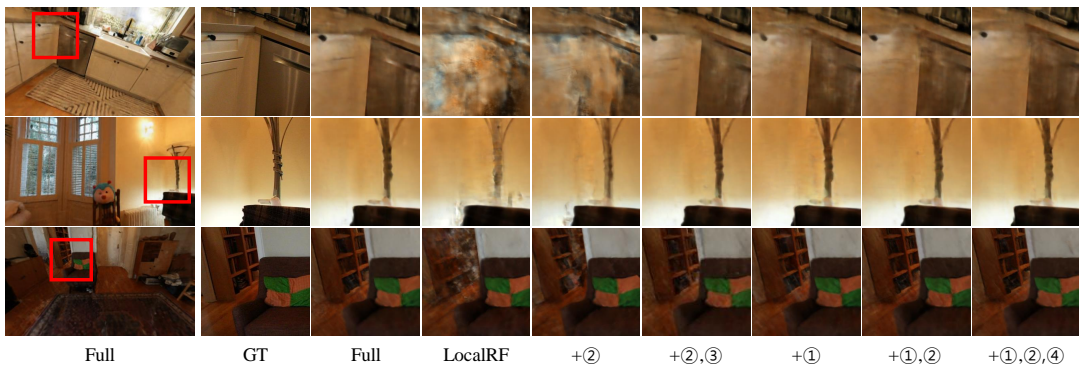


Figure 12. Qualitative results for ablation study on Zip-NeRF [2] dataset.

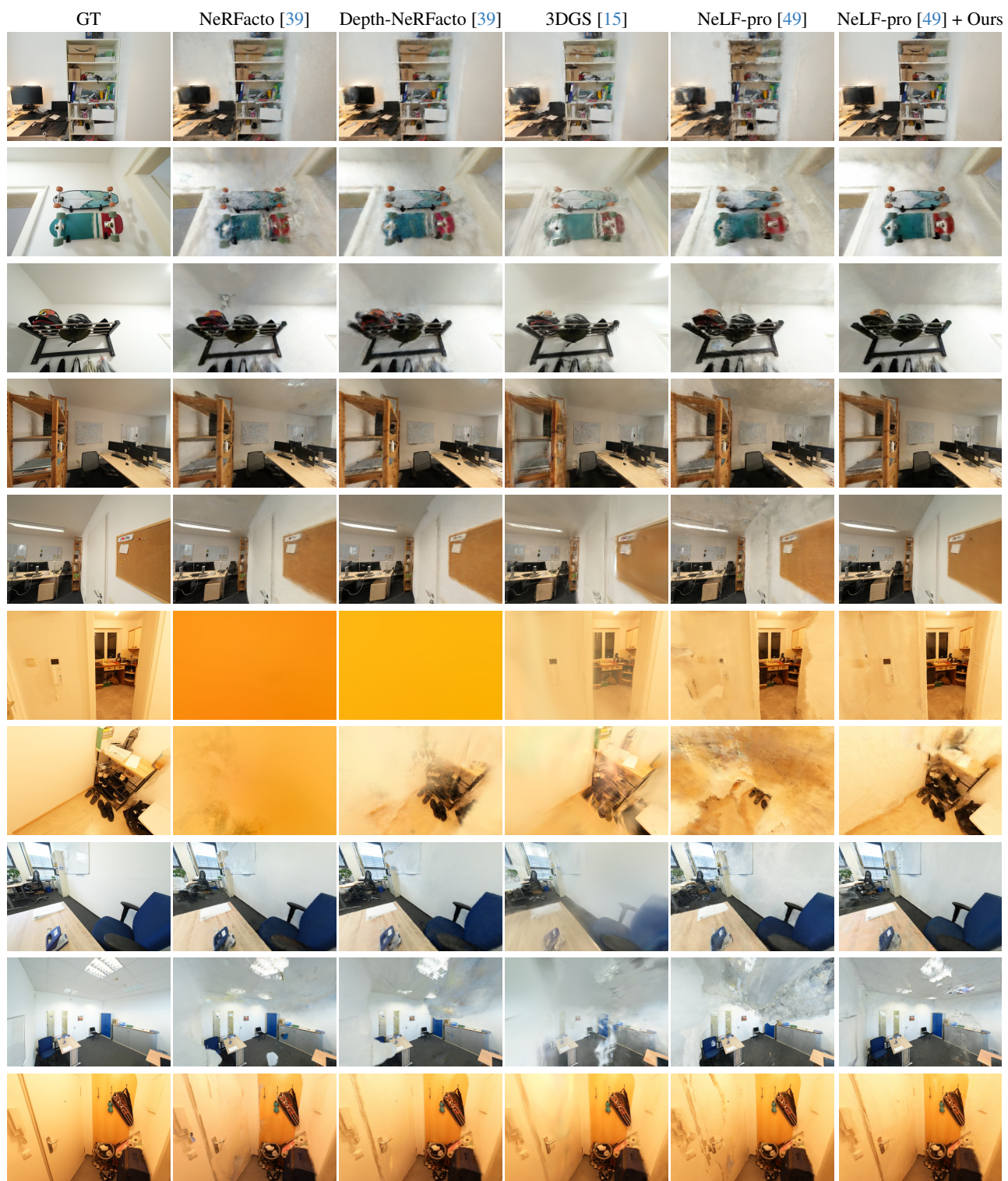


Figure 13. Additional visualizations of novel view synthesis results on ScanNet++ [48] dataset.

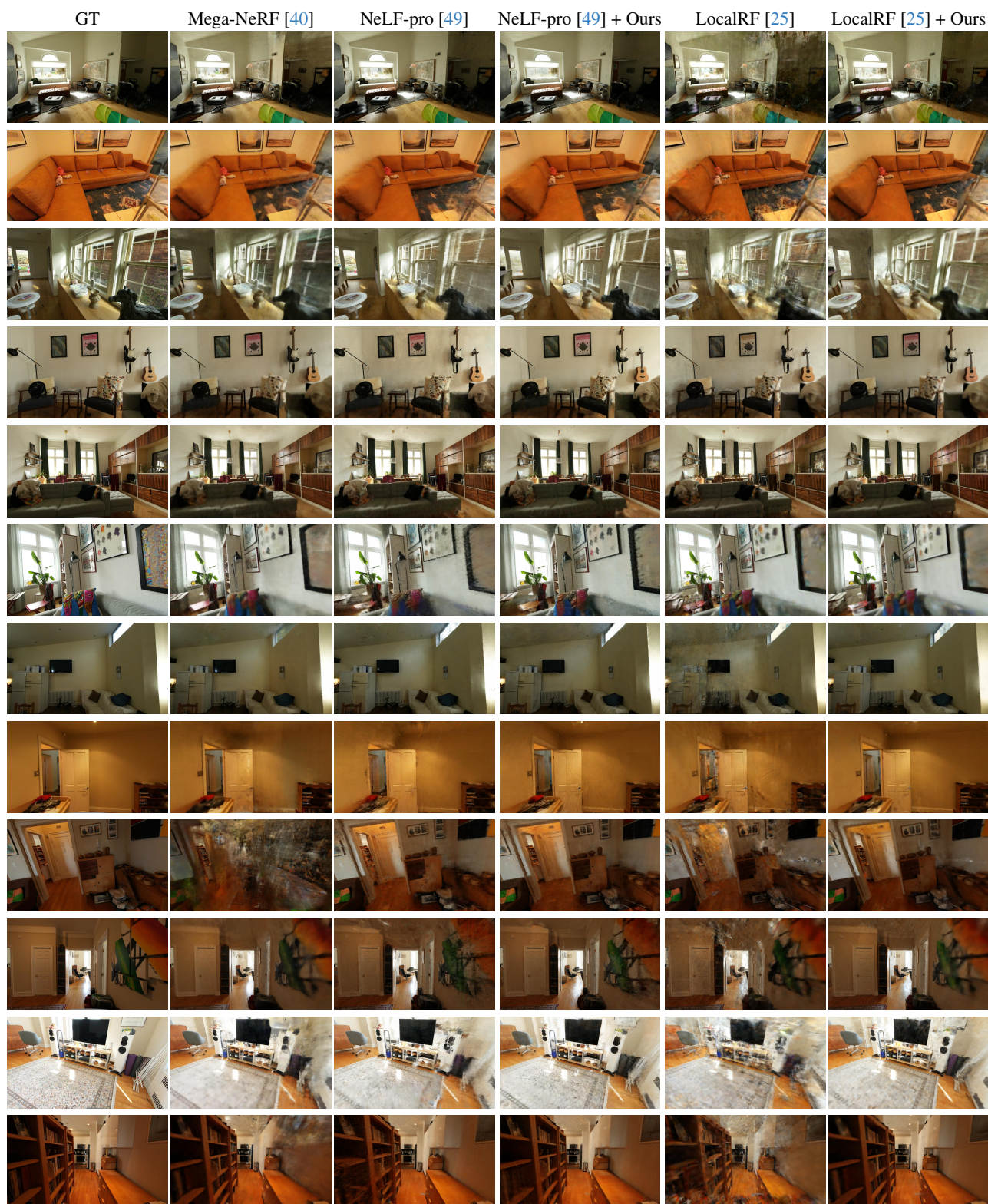


Figure 14. Additional visualizations of novel view synthesis results on Zip-NeRF [2] dataset.